International
Progress Report

IPR-05-36

Äspö Hard Rock Laboratory

TRUE Block Scale continuation project

Evaluation of the BS2B sorbing tracer tests using the Posiva streamtube approach

Antti Poteri

VTT Processes

August 2005

Svensk Kärnbränslehantering AB
Swedish Nuclear Fuel
and Waste Management Co
Box 5864
SE-102 40 Stockholm Sweden
Tel 08-459 84 00
+46 8 459 84 00
Fax 08-661 57 19
+46 8 661 57 19

Äspö Hard Rock
Laboratory

Report no.
IPR-05-36
No.
F56K
Author
Antti Poteri
Date
August 2005
Checked by
Anders Winberg
Date
September 2006
Approved
Anders Sjöland
Date
2006-11-29

Äspö Hard Rock Laboratory

TRUE Block Scale continuation project

Evaluation of the BS2B sorbing tracer tests using the Posiva streamtube approach

Antti Poteri

VTT Processes

August 2005

Keywords: Fault, Fracture, Heterogeneity, In-situ, Prediction, Retention, Sorbing, Tracer

Abstract

This report presents modeling work for predictions and evaluation of the BS2B tracer experiment of the TRUE Block Scale Continuation project. Tracer tests were performed along two flow paths using a variety of different sorbing tracers. Path lengths were over 20 m for both flow paths. In the flow path I the injection location was in the same fault type feature as extraction location (Structure #19). In the flow path II the injection was performed in the separate non-fault type background feature (BG1). The connection from BG1 to #19 is not known deterministically. The Euclidean distance from injection location to extraction location is in this case about 20 m, but the actual path length is probably longer because BG1 and #19 are subparallel.

A blind prediction of the tracer test outcome was performed prior to the evaluation of the experiment. The prediction was based on the given micro-structural model of the immobile pore space along the flow paths, results of the non-sorbing tracer tests and dilution measurements of the flow rates at the injection locations. Predictive modelling showed too much retention for sorbing tracers.

Evaluation of the tracer tests indicates that effective immobile zone retention properties are stronger along the flow path I, which goes along the associated fault type fracture. Effective immobile zone retention properties along the flow path II (injection at the non-fault fracture) seems to be dominated by the properties of non-fault background fractures. An interesting observation of the evaluation has been that a model of single unlimited immobile zone with sorption and matrix diffusion works very well for all breakthrough curves. Evaluation has showed that very distinct layers of different materials at a centimetre scale (thickness of the material layer) should manifest themselves in the breakthrough curves of the non-sorbing tracers at the experimental time scale of BS2B.

Sammanfattning

Denna rapport presenterar prediktioner och utvärderingsmodellering av spårförsök med sorberande spårämnen BS2B inom ramen för projektet TRUE Block Scale Continuation. Spårförsöken genomfördes i två flödesvägar med utnyttjande av olika sorberande spårämnen. Flödesvägarnas längd översteg båda 20 meter. För flödesväg I ligger både injektions- och pumpsektion i samma förkastningstruktur (Struktur #19). I flödesväg II skedde injektionen i en ”bakgrundsspricka” (BG-1) utan förkastningskaraktär med pumpning i Struktur#19. Den exakta hydrauliska kopplingen mellan BG-1 och Struktur#19 är inte känd deterministiskt. Det Euklidiska avståndet mellan injektions- och pumpsektion är i detta fall 20 m, men den faktiska flödesvägen är förmodligen längre givet att BG-1 och Struktur #19 är subparallella.

En ”blind” prediktion av utfallet av spårförsöket genomfördes före in-situförsöket och före utvärderingen. Prediktionerna baserades på den givna mikrostrukturella modellen av den immobila porstrukturen längs flödesvägarna, resultat från föregående försök med icke-sorberande spårämnen och flödeshastigheter i injektionssektionerna som erhållits från utspädningsförsök.

Utvärdering av spårförsöken visar att de effektiva retentionsegenskaperna hos de immobila zonerna längs flödesvägarna är högre längs flödesväg I som utgörs av en struktur med uttalad förkastningskaraktär. De effektiva retentionsegenskaperna längs flödesväg II (injektion i en struktur som saknar förkastningskaraktär) verkar bestämmas av egenskaperna hos bakgrundssprickor (som saknar förkastningskaraktär). En intressant observation från utvärderingen är att en modell med en enskild oändlig immobil zon med sorption och matrisdiffusion verkar förklara samtliga genombrottskurvor. Utvärderingen visar vidare att distinkta lager av olika material i centimeterskala (tjockleken hos enskilda lager) borde manifestera sig i genombrottskurvorna för icke-sorberande spårämnen för de experimentella tidsskalor som använts i BS2B försöken.

Contents

1 Introduction **9**

2 Objectives **11**

3 Flow paths **13**
3.1 Description of fracture network 13
3.2 Description of pore space 15

4 Pre-tests **19**

5 Basis for predictive modelling **21**
5.1 Flow model 21
5.2 Transport model 23
5.2.1 Processes considered 23
5.2.2 Mathematical description 24
5.2.3 Numerical implementation 28
5.2.4 Parameters 28
5.3 Model fitting using CPT-4C pre-test results 31

6 Model predictions and comparison with BS2B results **35**

7 Evalution **41**
7.1 Processes considered in the evaluation 41
7.2 Behaviour of the different tracers 42
7.3 Response functions of the different tracers 44
7.4 Flow field and hydrodynamic control of retention 50
7.5 Results for the BS2B micro-structural model 52
7.6 Results for the case of varied fault gouge 55
7.7 Results for the case of altered zone and intact rock only 60

8 Discussion **63**

9 Conclusions **67**

10 References **69**

1 Introduction

TRUE Block Scale Continuation (BS2) Project is a continuation of the TRUE Block Scale tracer test programme performed in a network fractures at a scale of tens of metres (Winberg, 1997). The overall objective of BS2 can be summarised as: “Improve understanding of transport pathways at the block scale, including assessments of effects of geometry, macrostructure, and microstructure”.

The second phase of the TRUE Block Scale Continuation Project comprised of a set of sorbing tracer tests, the BS2B experiment. This report presents the Posiva-VTT evaluation of the BS2B sorbing experiment. This phase of the project also included blind predictions of the BS2B sorbing tracer tests that are also presented in this report.

2 Objectives

This study both presents the predictions made for the sorbing tracer tests of the TRUE Block Scale Continuation project and the subsequent evaluation of the tracer tests. The principal for the analysis is an assumption that the important retention processes invoked by the experiment are sorption and matrix diffusion. The main objectives of this study can be condensed in following points:

- Reporting of prediction work
- Evaluation of BS2B tests on the basis of variable flow and matrix diffusion. This work takes into account sorption and the recommended micro-structural model of the immobile pore space.
- Evaluation of the relative role of the flow field and micro-structural model using alternative models.

3 Flow paths

3.1 Description of fracture network

The pumping section employed in the pre-tests (CPT-4C) and BS2B sorbing tracer tests has been the intersection point of Structure #19 in borehole KI0025F03. Two different injection sections have been used. Both injection sections are located in the borehole KI0025F02. One is in the same hydraulic feature as the extraction borehole, Structure #19. This flow path is here denoted flow path I. The second one is in the background fracture named BG1. This fracture is sub-parallel to Structure #19. This flow path is here denoted flow path II.

Figure 3-1 shows the overall geometry that has been applied in the tests. Figure 3-2 and 3-3 show the flow paths from different angles and at variable scale. The distance between the injection and extraction points in the Structure #19 (flow path I) is about 20 m. The length of the flow path from BG1 to the extraction borehole is not known explicitly. In this study it is assumed that the connection from BG1 to the extraction borehole takes place directly by way of BG1 alone. Extending BG1 to intersect the Structure #19 indicates that the path length along BG1 to the Structure #19 is about 15 m, although the shortest distance from BG1 injection point to the Structure #19 is only 3.3 m (i.e. BG1 and the Structure #19 are subparallel). The path length along the Structure #19 to the sink from the assumed intersection of BG1 and the Structure #19 is about 23 m. The distance from the source in BG1 to the sink is about 22 m, i.e. the projected path length along BG1 to the Structure #19 and then the added distance along the Structure #19 to the sink is 15 m + 23 m = 38 m that is almost twice the distance from source to sink. Predictions were calculated using the assumption that the path length along Structure #19 is 20 m for both flow path I and flow path II. The path length along BG1 for the flow path II is also assumed to be about 20 m. This makes the lengths of the flow paths to be about 20 m for flow path I and about 40 m for flow path II. It is again stressed that details of the connection and the length of the path from BG1 to Structure #19 is not fully known.

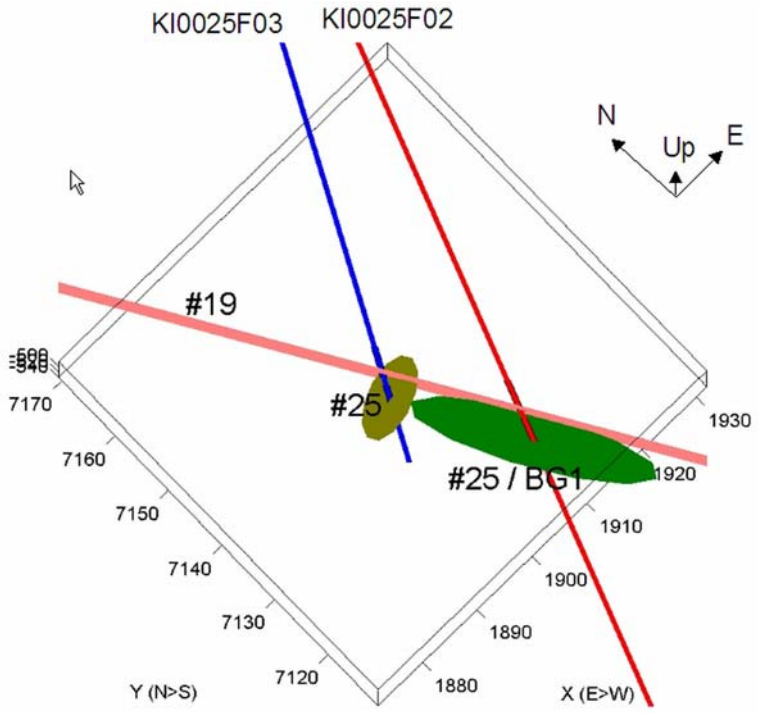

Figure 3-1. *Horizontal cross-section of the BS2B area. View is downward from the upper south-west corner of the BS2B block (in the figure south-west is at the bottom and north-east at the top). Extraction borehole KI0025F03 (blue) and injection borehole KI0025F02 (red). Structure #19 is indicated by pink plane and BG1 (green). Originally BG1 was named as Structure #25 that was also identified in borehole KI0025F03. This intersecting feature is also indicated in the figure (light green).*

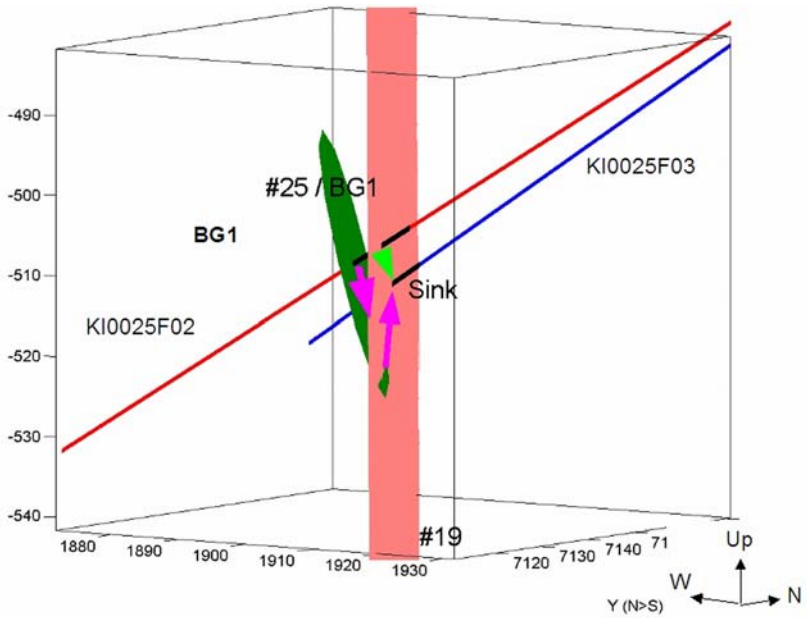

Figure 3-2. *Vertical cross-section of the area of BS2B test showing injection (red) and sink (blue) boreholes together with the Structure #19 and fracture BG1. The view is horizontally from south-east towards north-west. Flow path I is shown by a green arrow and flow path II by a magenta-coloured arrow.*

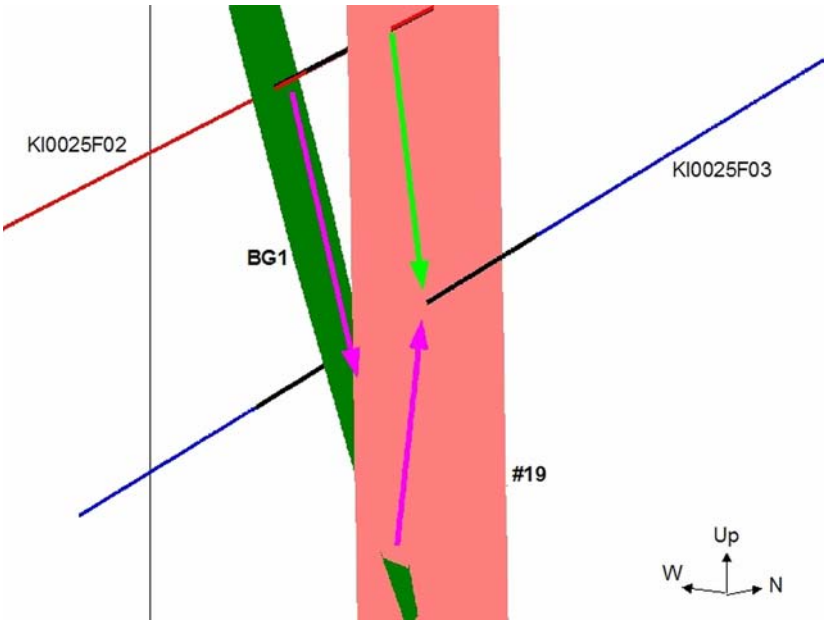

Figure 3-3. *Close-up of the Figure 3-2. Vertical cross-section of the BS2B area showing injection and sink (blue) boreholes together with the Structure #19 and fracture BG1. The view is horizontally from south-east towards north-west. Flow path I is shown by a green arrow and flow path 2 by magenta-coloured arrows.*

3.2 Description of pore space

Distribution of the immobile pore space has been defined for the structures in the BS2 experimental area (Tullborg and Hermanson, 2004). Definition of the immobile pore space follows the approach applied in Task 6 of the Äspö Task Force (Dershowitz et al., 2003). The hydraulic structures involved in the experiment are divided in two different classes named “Type 1” and “Type 2”. Type 1 is a fault type feature and Type 2 is a non-fault type feature. The immobile pore space in both types is made up of layers of different pore spaces as shown in Figure-34. Tullborg and Hermanson (2004) have interpreted that Structure #19 is a fault type feature (Type 1) and fracture BG1 is a non-fault type feature (Type 2). Material property parameters for the different layers making up the structure types are given in the Table 3-1.

Figure 3-4 also shows that the layers are always arranged in an order of decreasing porosity, for example, there is no coating at the top of fault gouge (cf. also coating, cataclasite and gouge to e.g. altered rock). In the current evaluation model the microstructural model is equated by an equivalent system of more symmetric pore space structure as shown in the Figure 3-4.

The micro-structural model also includes a characteristic called the complexity factor. This indicates the number parallel water conducting fractures in the structure. In Structure #19 the complexity factor varies from 1 to 3 and for BG1 it is 1. However, in the current modelling both features are assumed to contain one water conducting fracture. This is based on the observation that the flow rate usually distributes unevenly between parallel fractures. This means that from a transport point of view one of the subparallel water conducting fractures dominates. This is also supported by the usually applied estimate that fracture transmissivity depends on the cube of the fracture aperture.

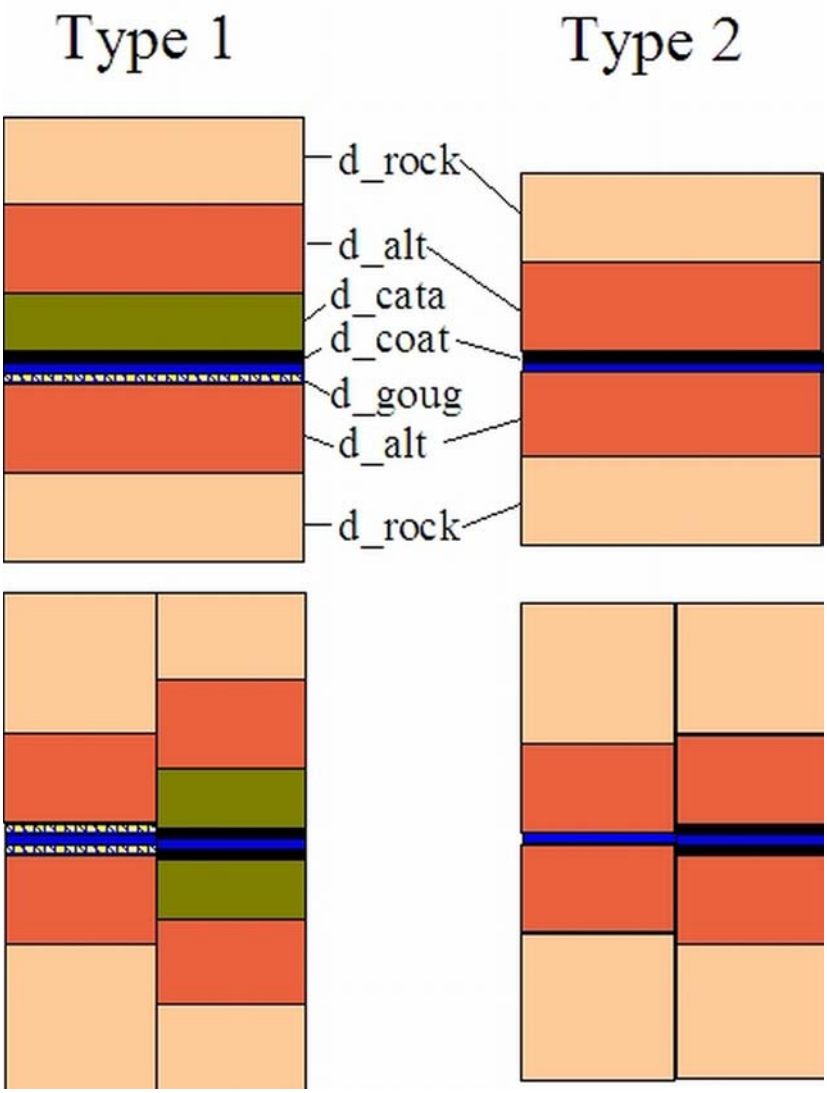

Figure 3-4*. Hydraulic features are classified in two different types according to the internal structure of the immobile pore space. The micro-structural model of the different structure types is composed of layers of different geological materials. The notation of the Type 1 and Type 2 structures are shown at the top. Representation of the Type 1 and Type 2 features in the current evaluation model is shown at the bottom of the figure. The model cannot directly handle the original asymmetric distribution of the immobile pore space (e.g. coating and gouge). It is represented in the current model by an equivalent but more symmetric structure as shown at the bottom of the figure. From transport point of view these two representations are equivalent (retention by matrix diffusion is the same).*

Table 3-1. Properties of the immobile pore space for Type 1 and Type 2 structures (Tullborg and Hermanson, 2004), cf. Figure 3-4.

Type 1 (fault)			
Rock type	**Extent [cm]**	**Porosity [%]**	**Formation factor [-]**
Intact wall rock(d_rock)	-	0.3	7.3e-5
Altered zone (d_alt)	15	0.6	2.2e-4
Cataclasite (d_cata)	1	1	4.9e-4
Fault gouge (d_goug)	0.3	20	5.6e-2
Fracture coating (d_coat)	0.05	5	6.2e-3
Type 2 (non-fault)			
Rock type	**Extent [cm]**	**Porosity [%]**	**Formation factor [-]**
Intact wall rock (d_rock)	-	0.3	7.3e-5
Altered zone (d_alt)	5	0.6	2.2e-4
Fracture coating (d_coat)	0.05	5	6.2e-3

4 Pre-tests

A set of pre-tests were conducted prior and in preparation to the actual sorbing BS2B tracer tests. The same pumping configuration as in the subsequent BS2B sorbing tracer tests was employed in tests CPT-4B (flow path II) and CPT-4C (both flow path I and II). In addition, dilution tests CPT-3C employed the same pumping borehole section as the BS2B tests and the injection sections of the BS2B tests were also investigated in the CPT-3C experiment.

The prediction work was based on the data of the dilution tests (CPT-3C) and the CPT-4C pre-test. Results from the CPT-4B test were not used in the predictions.

The average pumping rate in KI0025F03:R3 was 2.68 l/min in CPT-4B and 2.56 l/min in CPT-4C. The pumping rate during the BS2B sorbing test was in the same order of magnitude, i.e. about 2.5 l/min. All tracer tests have been performed as weak dipoles where the injection of water has been 2.0 ml/min in BG1 and 5.0 ml/min in Structure #19. In the present modelling approach the flow conditions along the flow paths are determined from the background flow field. Therefore, the injection flow rate at the injection borehole is not important as long as the dipole weak. The background flow field along the flow paths is determined from the CPT-3C dilution tests.

Figures Figure 4-1 to Figure 4-3 present the injection and breakthrough curves for the CPT-4B and CPT-4C tests. Results of the dilution tests CPT-3C are presented in Section 5.1.

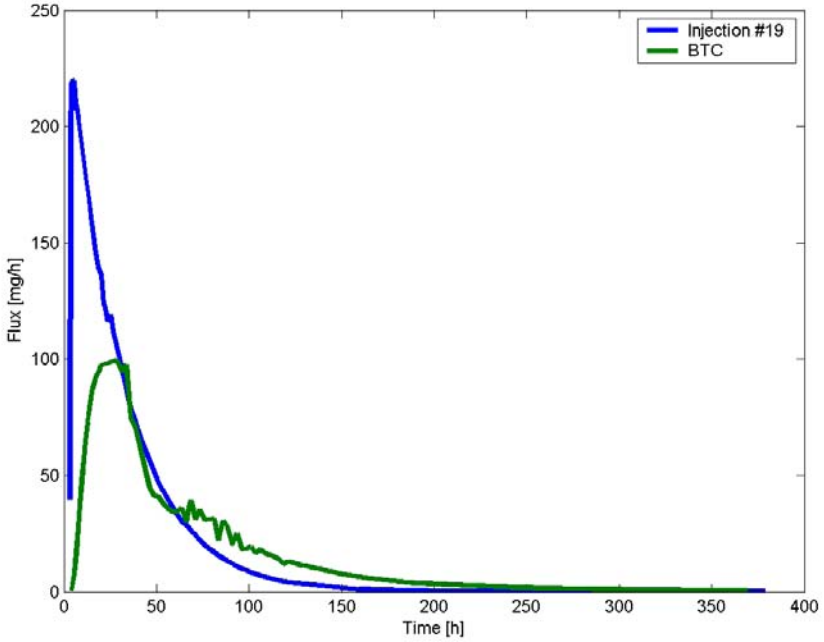

Figure 4-1*. Injection and breakthrough curves for the flow path I in CPT-4C test (injection in the Structure #19).*

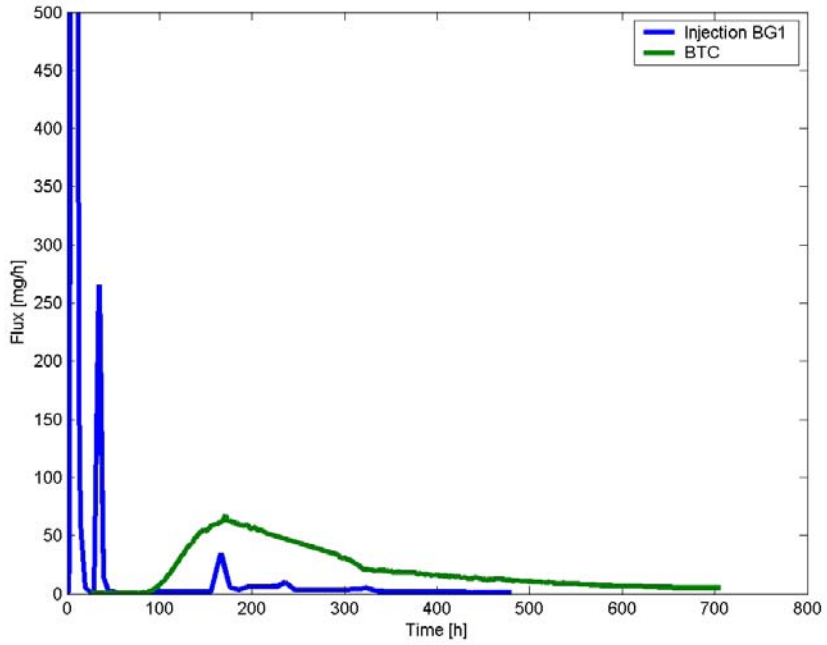

Figure 4-2. *Injection and breakthrough curves for flow path II in CPT-4C test (injection in BG1). The first peak of the injection curve is cut in this figure. The maximum injection rate is about 2300 mg/h.*

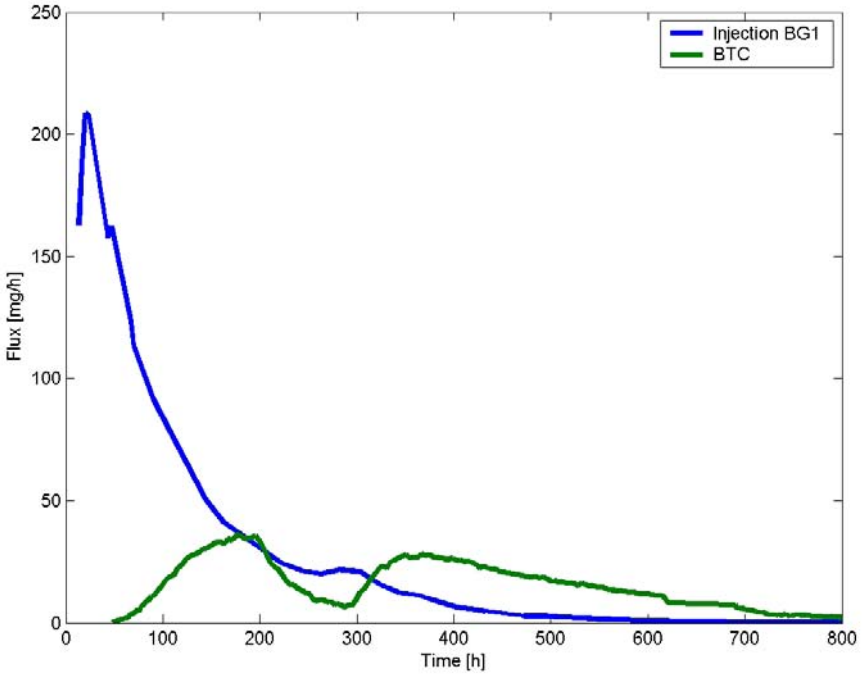

Figure 4-3. *Injection and breakthrough curves for flow path II in CPT-4B test (injection in BG1).*

5 Basis for predictive modelling

5.1 Flow model

The prediction model is based on a very simple flow model applied for steady state flow conditions. It is assumed that the flow rate through the main flow channels can be deduced from the results of the tracer dilution tests made in the BS2B injection locations in Structure #19 and BG1, respectively. A significant simplification of the prediction model is that only the average flow rate (bulk flow) is used for the whole transport path, i.e. variable flow along the flow path is not taken into account. The characteristic of the flow field that is of interest in this modelling is β (c.f. Equation (5-4)) that is roughly determined based on the tracer dilution experiments and geometric estimates of the lengths of the transport paths.

Modelling of the flow field is based on the assumption that the flow field of the injected tracer plume adapts itself to the background flow field. This is motivated by the following consideration. The injection flow rates are low (Table 5-1) so that they will probably only cause a very local influence on the flow field, which is created by the pumping in the extraction borehole and the background flow field caused mainly by the open tunnel. It is also assumed that there are no geometrical limitations for the flow close to the injection boreholes. This means that the solution injected from the borehole may spread to the surrounding flow field quite freely (note that the diameter of the borehole is only few centimetres and that the injection flow rates are small). Figure 5-1 shows an illustrative example of this kind of situation. It shows a linear background flow field through a homogeneous (infinite) fracture where water is injected to the fracture through a borehole. The assumptions presented above hold for this example and indeed after a short transition zone the flow field inside the transport channel (area between the red streamlines in Figure 5-1) does not differ from the background flow field.

The approach presented above is applied for robust estimation of the hydrodynamic control of the retention (β) that is represented by the entity $W \cdot L/Q = \beta/2$ in this report (where W is the width, L is the length and Q is the flow rate in the transport channel). Lengths of the transport paths are based on the geometric considerations presented in Section 3.1. Flow conditions at the injection locations in the field are used for estimation of the average Q/W along the transport paths. A sample of the Q/W at the injection locations can be taken from the tracer dilution measurements made under the same pumping conditions as the BS2B experiment. Table 5-2 shows the results of the CPT-3C dilution tests. As explained in the preceding chapter it is assumed that representative flow conditions (Q/W) along a flow path are mainly determined by the flow at the injection location, i.e. in a case of weak dipole the injection flow rate is not that important (case $Q_{stressed}$ in Table 5-2).

The pumping rate has been about 2.5 l/min in BS2B and about 2.84 l/min in CPT-3C. This is taken into account by scaling the influence of the pumping on the flow in flow path I (scaling indicates about 68 ml/h instead of 76 ml/h). Now assuming the flow rate measured in the tracer dilution test represents the flow rate over a width of about 0.1 m (the borehole diameter is about 0.076 m) gives Q/W. Rough estimates of the WL/Q for the flow paths are for the flow path I, WL/Q = 0.1 m*22 m/(68 ml/h) = 10^8 s/m, and for

flow path II, WL/Q = 0.1 m*20 m/(42 ml/h) + 0.1 m*20 m/(68 ml/h) = $3 \cdot 10^8$ s/m, where the legs of the flow path along BG1 and Structure #19 are given separately. Finally, the WL/Q values for the flow paths are calibrated by fitting the breakthrough curves of the non-sorbing CPT-4C tracer test, but the above values are used as guidance. The rough estimates of the WL/Q given above show a factor of 2 to 3 difference to the evaluated WL/Q values (cf. Table 7-2).

The CPT-3C tracer dilution tests also show that the natural background flow field dominates in BG1. The flow rate in injection section KI0025F02:R2 (BG1) does not change whether the extraction borehole section (KI0025F03:R3) is pumped or not. On the other hand, pumping does influence the flow rate at the injection section in Structure #19. The flow field can be studied by comparing the measured change in flow rate with the flow rate calculated from the pumping rate and distance from the injection location to the sink (about 20 m). Uniform distribution of the pumping rate at the sink over the circumference of a 20 m circle gives a flow rate of about 136 ml/h over 10 cm (this is assumed to represent the diameter of the borehole in the dilution test). In the in situ dilution tests the measured flow rate is clearly smaller, 58 ml/h (or 94 ml/h, because the direction of the flow through the borehole is not known), indicating that there might be other connections to the sink that give more water than the connection towards the injection point in the BS2B experiment.

Table 5-1. Specification of the BS2B tests (Andersson et al., 2005).

	Source/Structure	**Pumping rate (ml/min)**	**Tracers**	**Euclidean Distance (m)**
Sink	KI0025F03:R3 / #19	2300-2500		0
Injection	KI0025F02:R3 / #19	5.0	$^{131}I^-$, $^{160}TbDTPA^{2-}$, $^{85}Sr^{2+}$, $^{86}Rb^+$, $^{137}Cs^+$	19.5
Injection	KI0025F02:R2 /BG1	2.0	HTO, $^{155}EuDTPA^{2-}$, $^{22}Na^+$, $^{133}Ba^{2+}$, $^{54}Mn^{2+}$	22

Table 5-2. Results of the CPT-3C dilution tests for the borehole sections that have been used in the BS2B tests. The flow rate in the sink was 2.84 l/min (case $Q_{stressed}$). Data have been taken from Andersson et al. (2004).

Test section	**Structure #**	**Distance (m)**	**$Q_{natural}$ (ml/h)**	**$Q_{stressed}$ (ml/h)**	**ΔQ (ml/h)**
KI0025F03:R3	19	0	SINK: 170 400 ml/h (2.84 l/min)		
KI0025F02:R3	19	20	18	76	+ 58
KI0025F02:R2	BG1	22	42	42	± 0

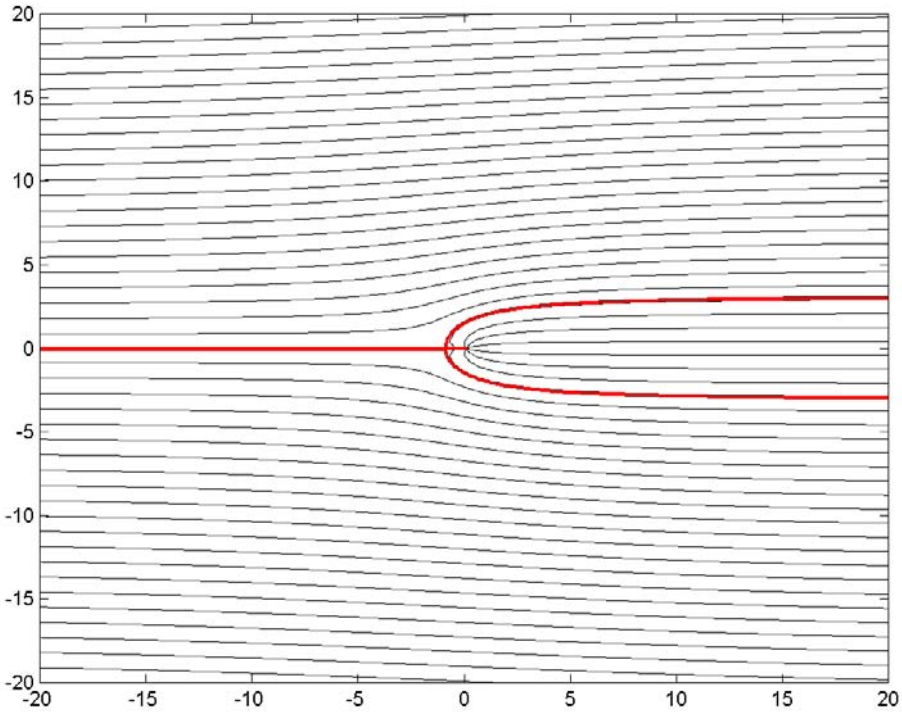

Figure 5-1. *Illustration of how a tracer plume pumped from a borehole adapts itself to background flow. The figure shows streamlines for a flow field over a (infinite) homogeneous fracture (thin black lines). The flow field is composed of a linear background flow and injection from the borehole. Red lines show the streamlines that pass the borehole so that an injected plume remains between the red lines, i.e. the developed transport channel (no molecular diffusion taken into account). Flow rate can be deduced from the density of the streamlines. It can be seen that the flow field in the transport channel adapt itself to the background flow field already quite close to the injection point; the density of the streamlines at the right and left vertical edges of the domain are almost identical.*

5.2 Transport model

5.2.1 Processes considered

Transport model takes into account advection along the fractures, matrix diffusion and sorption in the immobile pore space. Surface sorption on the fracture walls was not modelled, but the diffusion into the pore space of the fracture coating and sorption in the pore space of the coating were directly modelled.

The connection from the source to the sink was described by one transport path for each of the injections. In the prediction model there is no variable advection inside a given transport path. Hydrodynamic dispersion was included only to the evaluation model.

5.2.2 Mathematical description

Transport of the tracers is described by applying the advection – matrix diffusion equation

$$\begin{aligned} & R_a \frac{\partial c_f}{\partial t} + v \frac{\partial c_f}{\partial x} - 2 \frac{D_e}{2b} \frac{\partial c_m}{\partial z}\bigg|_{z=0} = 0 \\ & R_p \frac{\partial c_m}{\partial t} - D_p \frac{\partial^2 c_m}{\partial z^2} = 0 \end{aligned} \quad , \tag{5-1}$$

where *Ra* is the retardation coefficient of the surface sorption (*Ra*=1 for all tracers in this modelling, i.e. surface sorption is not taken into account in this modelling). Matrix concentration $c_m(x,z,t)$ and fracture concentration $c_f(x,t)$ are coupled by the requirement that $c_m(x,0,t) = c_f(x,t)$. Initial concentration is zero both in the matrix and in the fracture.

The Laplace transform of the equation (5-1) gives

$$\begin{aligned} & R_a s \bar{c}_f + v \frac{\partial \bar{c}_f}{\partial x} - 2 \frac{D_e}{2b} \frac{\partial \bar{c}_m}{\partial z}\bigg|_{z=0} = 0 \\ & R_p s \bar{c}_m - D_p \frac{\partial^2 \bar{c}_m}{\partial z^2} = 0 \end{aligned} \quad , \tag{5-2}$$

where *s* is the variable of the Laplace domain. Equation (5-2) indicates that the solution could be sought using product $\bar{c}_m(x,z,s) = f(z)\bar{c}_f(x,s)$ with $f(0) = 1$. This leads to a solution

$$\bar{c}_f(x,s) = C_o \, \mathrm{Exp}\left(-\frac{R_a \, s \, x}{v} + \frac{2 \, x \, D_e}{2b \, v} \, f'(0) \right) , \tag{5-3}$$

where *Co* is determined by the source term at the inlet of the flow path (e.g. for step input $c_o \, H(t)$, where *H* is the Heaviside's step-function, it is $C_0 = c_0 / s$. For the Dirac pulse injection $M_0 \delta(t)$ it is $C_0 = \frac{M_0}{W(2b)v} \delta(t)$, where *W* is the width of the flow channel.). Boundary conditions in the immobile pore space of the rock matrix are taken into account by the second equation of (5-2) and they emerge in the solution of the breakthrough curve through the term *f'(0)* (cf. equation (5-3)). For one homogeneous layer of immobile pore space we get

$$\begin{aligned} & \frac{2 \varepsilon D_p}{2b v} \, f'(0) = \\ & = -2\sqrt{s} \, \frac{x}{v \, 2b} \, \varepsilon \sqrt{D_p R_p} \, \tanh\left(L \sqrt{s \, R_p / D_p} \right) \\ & = -\sqrt{s} \, \beta \, \gamma \, \tanh\left(L \sqrt{s \, R_p / D_p} \right) \end{aligned} \quad , \tag{5-4}$$

where $\beta = x/(v\,b)$ determines the flow conditions in the transport channel, $\gamma = \varepsilon\sqrt{D_p R_p}$ determines the properties of the immobile region and L is the thickness of the immobile pore space. This shows that two different immobile regions give the same retention (breakthrough curve) if they have the same γ and $L\sqrt{R_p / D_p}$, i.e. the same grouped matrix properties and the same "diffusion time" through the immobile layer.

Solute transport through the system of layered immobile zones is calculated by constructing an equivalent system of successive flow paths that have homogeneous immobile regions. This can be done if the diffusion property of the immobile layers, i.e. γ, is always smaller for the layer that is deeper in the rock matrix. This is the case in the Type 1 and Type 2 features and for the tracers applied in the BS2B tests. The different layers both in Type1 and Type 2 features form a series of decreasing γ from the fracture coating into the intact rock. The modelling approach is explained more in detail below.

Let us first consider a case where there are two different layers of the immobile pore space that differ only by the porosity (Figure 5-2a). We may conceptualise the connected porosity that is accessible by diffusion from the fracture as 1D pipes (Figure 5-2b). Next, we may arrange the pipes along the flow path so that first there are the long pipes and then the shorter pipes (Figure 5-2c). Changing the order of the pipes does not affect the solute transport, because if the flow path is composed of separate legs then the total output is a convolution between the outputs of the individual legs and the convolution is a commutative operation. This means that a flow path with two layers of immobile pore space is equivalent to a system of two successive flow paths that both have one layer of the immobile pore space according to Figure 5-2d. Note, that this is possible only if $\varepsilon_2 < \varepsilon_1$.

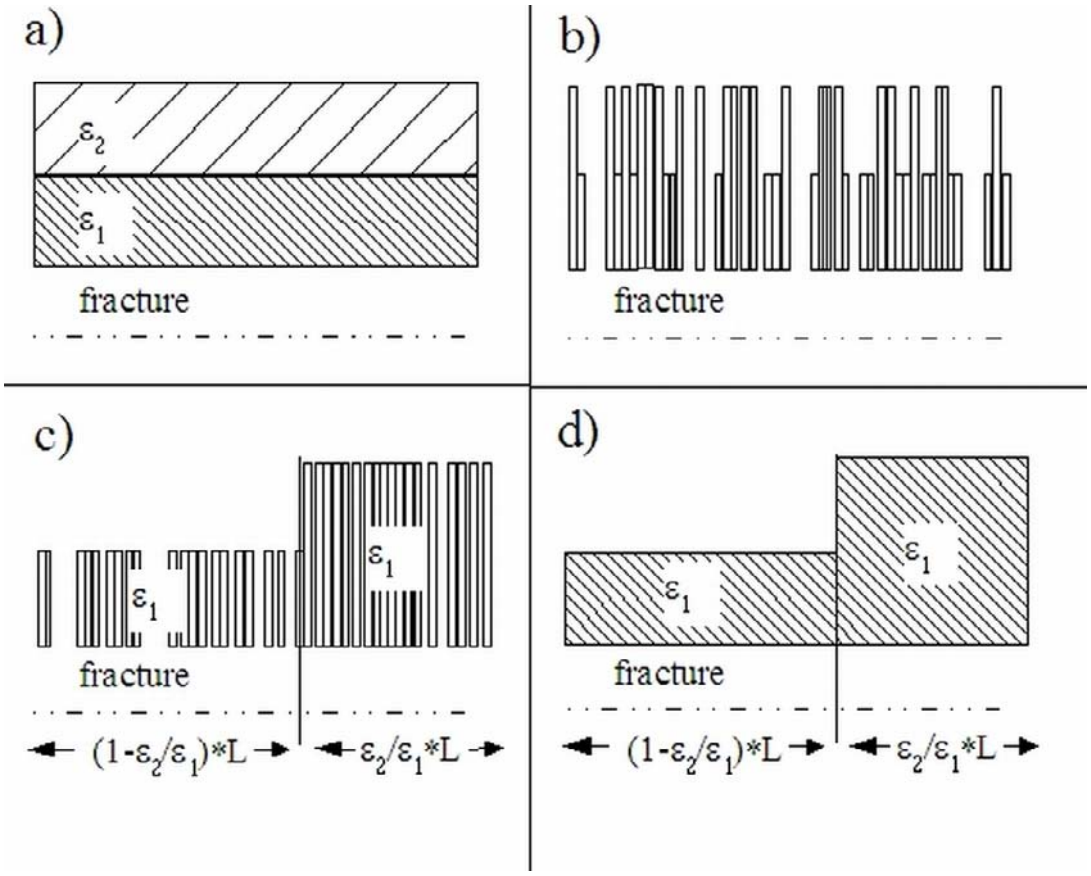

Figure 5-2. *Illustration of a flow path along a fracture that is in contact with a heterogeneous immobile pore space. The immobile pore space is composed of two layers that have different porosities ($\varepsilon_2 < \varepsilon_1$, figure a). Connected porosity is represented by 1D pipes (figure b). The 1D pores are rearranged to form two successive legs of flow paths that both have one layer of immobile pore space.*

The approach above can be extended to the cases where, in addition to the porosity, also diffusivity and sorption properties vary between the layers. According to equation (5-4) the breakthrough curve depends on the following parameters: β that describes the hydrodynamic control of the retention, γ that describes the properties of the immobile region and the "diffusion time" through the immobile layer, $\sqrt{T} = L\sqrt{R_p / D_p}$. This means that the breakthrough curves for two flow paths are identical if they have the same β, γ and $L\sqrt{R_p / D_p}$, although the individual ε, D_p, R_p and L of the immobile regions are different. This is illustrated in Figure 5-3. It shows a breakthrough curve for a transport path that has a groundwater transit time t_w=3 h and aperture 2b=1 mm. The immobile pore space and the tracers are described by two different sets of parameters so that γ and $L\sqrt{R_p / D_p}$ remain unchanged. Figure 5-3 shows that both parameterisations lead to the same breakthrough curves.

Let us now consider a transport path with two layers of immobile regions such that $\gamma_2 < \gamma_1$, i.e. the layer close to the fracture has a bigger γ. We may now assign the same D_p and R_p to the second layer as to the first one, but to keep the γ_2 unchanged by giving

a new porosity for the second layer such that $\gamma_2 = \varepsilon_2 \sqrt{D_{p2} R_{p2}} = \varepsilon'_2 \sqrt{D_{p1} R_{p1}}$.
Changing D_p and R_p of the second layer will affect the "diffusion time" of the second layer. This can be compensated by changing the thickness of the second layer by the factor of $\sqrt{D_{p1} / R_{p1}} \Big/ \sqrt{D_{p2} / R_{p2}}$. It was originally required that $\gamma_2 < \gamma_1$, which means that $\varepsilon'_2 < \varepsilon_1$. After these modifications the two layer case, in which all parameters (D_p, R_p, ε and L) may have been different for different layers, is now represented by, in a transport sense, an equivalent system where the two layers vary only by the porosity. This means that the procedure shown in Figure 5-2 is also applicable for the general case assuming that $\gamma_2 < \gamma_1$ (cf. Figure 5-4).

It is straightforward to take the next step to a case with several immobile layers. First, to apply this procedure the diffusion properties through the immobile layers should change such that $\gamma_m < \gamma_n$ if the layer *m* is deeper in the fracture wall rock than the layer *n* (Figure 5-4). We divide the flow path into as many legs as there are immobile layers. Starting from the layer that has the smallest γ (layer that is furthest from the fracture) we immediately see that the location of the leg *m* along the flow path is $[\gamma_{m-1}/\gamma_1, \gamma_m/\gamma_1] \cdot L$, cf. Figure 5-4. The diffusion property of all legs is γ_1 and the thickness of the immobile layer *m* should be scaled by $L'_m = L_m \sqrt{D_{p1} / R_{p1}} \Big/ \sqrt{D_{pm} / R_{pm}}$ to keep the diffusion time unchanged (see Figure 5-4).

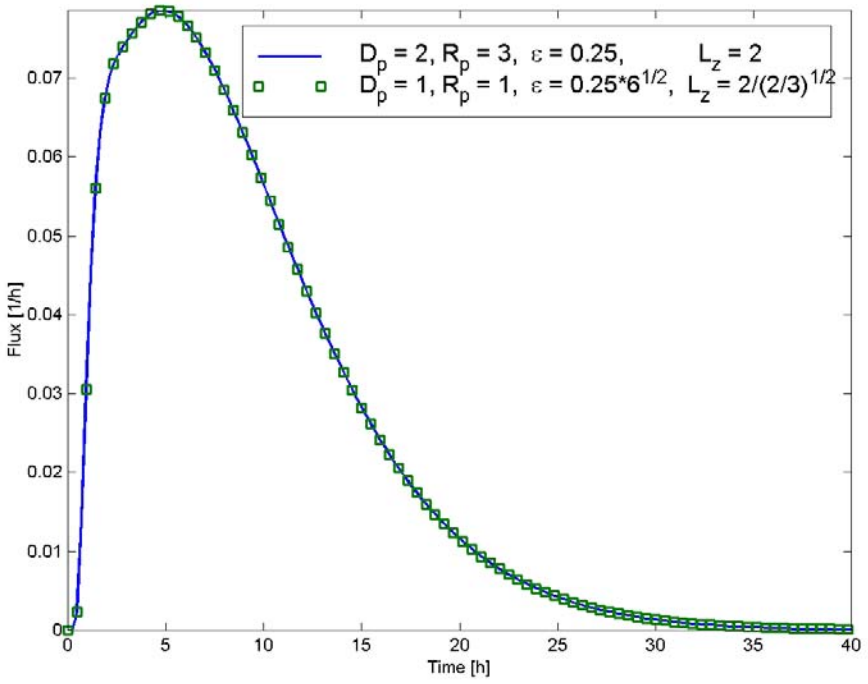

Figure 5-3. *Coinciding breakthrough curves for a transport path having properties t_w=1 h, 2b=1 mm and two different immobile layers. The results coincide because in both parameterisations $\gamma = \varepsilon \sqrt{D_p R_p}$ and the diffusion time through the immobile layer $t_{diff} = L_z^2 / (D_p / R_p)$ remain unchanged.*

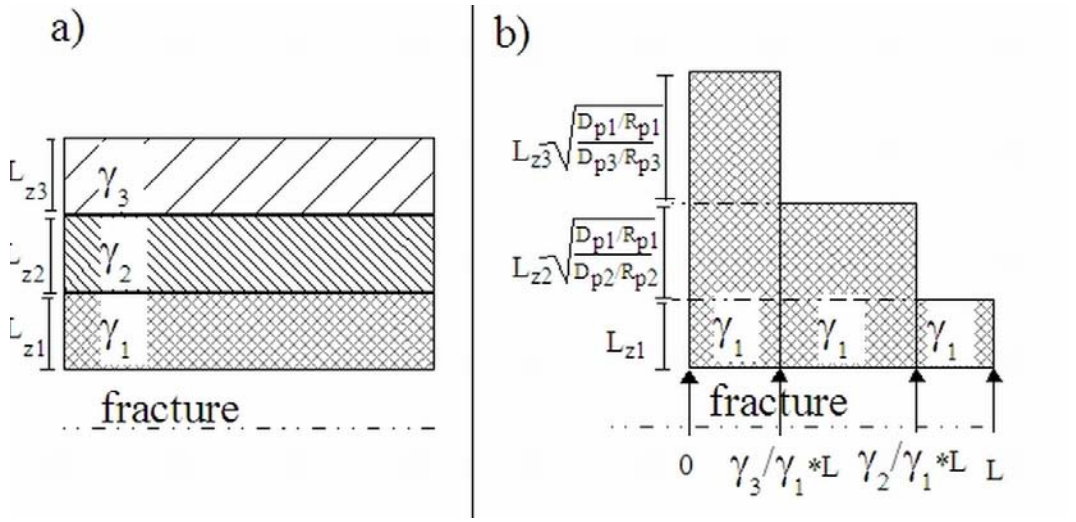

Figure 5-4. *Layered immobile pore space along a flow path (a) is divided into a sequence of flow paths that have homogeneous immobile pore space (b).*

5.2.3 Numerical implementation

Transport of tracer through a fracture that is surrounded by one layer of immobile pore space is calculated using an analytical model. It is based on a one-dimensional lattice walk where the interaction of the solute between the mobile and immobile pore space is described by a waiting time distribution that is applied at the grid points (Cvetkovic and Haggerty, 2002). However, in our approach the waiting time distribution is calculated directly in the time domain, not in the Laplace-domain as is done by e.g. Cvetkovic and Haggerty (2002).

The flow path is represented by a 1D lattice. The discretization is selected so that convergent results are achieved, but on the other hand the that calculation time is reasonable. Figure 3-4 shows that a flow path through both Type 1 and Type 2 feature is represented by two legs that have symmetric matrix properties (i.e. the structure of the matrix is the same on either side of the fracture). Following the approach presented in Section 3.3.2 both of these two legs, which have layered matrix properties, are represented by a series of flow paths with homogeneous matrix properties (cf. Figure 5-4). This means e.g. that the first part of the Type 1 feature in Figure 3-4 is represented by a series 3 flow paths (gouge, altered rock, intact rock) and the second part by a series of 4 flow paths (coating, cataclasite, altered rock, intact rock). This means that a flow path through a Type 1 feature should be represented by 7 successive legs. In the same way a Type 2 feature needs 5 successive legs.

Numerical calculations were carried using Matlab (Matlab, 2001).

5.2.4 Parameters

Transport parameters were based on the data given mainly by Byegård and Tullborg (2004). Some data that was not given in the memorandum by Byegård and Tullborg (2004) were taken e.g. from the definition of the Äspö Task Force Task 6C (Dershowitz et al., 2003) or estimated based on the data of other tracers. When calculating the retardation coefficients it was assumed that all geological materials have the same density of 2600 m^3/kg.

The sorption and diffusion data set applied in the calculations are presented in Table 5-3 and Table 5-4. Pore diffusivity calculated using porosity (Table 3-1) and diffusivity data (Table 5-4) are given in the Table 5-5. In addition, Table 5-6 shows the calculated γ values for different layers and different tracers. It can be seen that the micro-structural model shown as in Figure 3-4 does really exhibit a sequence of decreasing γ from the fracture surface to the inner parts of the matrix for all tracers.

Table 5-3. Sorption properties of geological materials (K_d [m3/kg]) for different tracers. Data are mainly based on Byegård and Tullborg (2004). Other sources of data are indicated by footnotes.

	Fracture coating (d_{coat})	Fault gouge (d_{goug}, concept A)	Cataclasite/ Mylonite (d_{cata}, 20%)	Altered zone (d_{alt}, #19)	Altered zone (d_{alt}, BG1)	Intact wall rock (d_{rock})
Uranine	0	0	0	0	0	0
Amino G	0	0	0	0	0	0
I	0	0	0	0	0	0
Tb-160	0	0	0	0	0	0
Sr	2.30E-04 [1)]	6.00E-04	1.40E-04	2.60E-05	2.60E-05	4.40E-05 [1)]
Rb	5.20E-03 [1)]	2.70E-03	4.00E-03	4.00E-04	4.00E-04	1.00E-03 [1)]
Cs	5.20E-02 [1)]	4.00E-02	3.00E-02	5.00E-04	5.00E-04	1.00E-03 [1)]
HTO	0	0	0	0	0	0
Eu-155	0	0	0	0	0	0
Na-22	2.00E-04	1.10E-04 [1)]	1.10E-05 [1)]	1.40E-05 [1)]	1.70E-06	7.10E-06 [1)]
Ba-133	2.72E-02	1.40E-02 [1)]	1.30E-03 [1)]	1.80E-03 [1)]	6.90E-04	8.80E-04 [1)]
Mn-54	1.70E-01	8.75E-02 [2)]	8.13E-03 [2)]	1.13E-02 [2)]	4.30E-03	5.48E-03 [2)]

[1)] Task 6C specification (Dershowitz et al., 2003)
[2)] Calculated based on Ba-133, i.e. the ratio between K_d's of Mn-54 and Ba-133 is same as for fracture coating.

Table 5-4. Diffusivities in free water, D_w [m^2/s]

	Fracture coating (d_{coat})	Fault gouge (d_{goug}, concept A)	Cataclasite /Mylonite (d_{cata}, 20%)	Altered zone (d_{alt}, #19)	Altered zone (d_{alt}, BG1)	Intact wall rock (d_{rock})
Uranine	5.00E-10	5.00E-10	5.00E-10	5.00E-10	5.00E-10	5.00E-10
Amino G	5.00E-10	5.00E-10	5.00E-10	5.00E-10	5.00E-10	5.00E-10
I	2.00E-09	2.00E-09	2.00E-09	2.00E-09	2.00E-09	2.00E-09
Tb-160	5.00E-10	5.00E-10	5.00E-10	5.00E-10	5.00E-10	5.00E-10
Sr	7.94E-10	7.94E-10	7.94E-10	7.94E-10	7.94E-10	7.94E-10
Rb	2.06E-09	2.06E-09	2.06E-09	2.06E-09	2.06E-09	2.06E-09
Cs	2.06E-09	2.06E-09	2.06E-09	2.06E-09	2.06E-09	2.06E-09
HTO	2.13E-09	2.13E-09	2.13E-09	2.13E-09	2.13E-09	2.13E-09
Eu-155	5.00E-10	5.00E-10	5.00E-10	5.00E-10	5.00E-10	5.00E-10
Na-22	1.33E-09	1.33E-09	1.33E-09	1.33E-09	1.33E-09	1.33E-09
Ba-133	8.48E-10	8.48E-10	8.48E-10	8.48E-10	8.48E-10	8.48E-10
Mn-54	6.88E-10	6.88E-10	6.88E-10	6.88E-10	6.88E-10	6.88E-10

Table 5-5. Pore diffusivities (D_p [m^2/s]) as calculated using D_w and porosities and formation factors given in Table 3-1.

	Fracture coating (d_{coat})	Fault gouge (d_{goug}, concept A)	Cataclasite /Mylonite (d_{cata}, 20%)	Altered zone (d_{alt}, #19)	Altered zone (d_{alt}, BG1)	Intact wall rock (d_{rock})
Uranine	6.20E-11	1.40E-10	2.45E-11	1.83E-11	1.83E-11	1.22E-11
Amino G	6.20E-11	1.40E-10	2.45E-11	1.83E-11	1.83E-11	1.22E-11
I	2.48E-10	5.60E-10	9.80E-11	7.33E-11	7.33E-11	4.87E-11
Tb-160	6.20E-11	1.40E-10	2.45E-11	1.83E-11	1.83E-11	1.22E-11
Sr	9.85E-11	2.22E-10	3.89E-11	2.91E-11	2.91E-11	1.93E-11
Rb	2.55E-10	5.77E-10	1.01E-10	7.55E-11	7.55E-11	5.01E-11
Cs	2.55E-10	5.77E-10	1.01E-10	7.55E-11	7.55E-11	5.01E-11
HTO	2.64E-10	5.96E-10	1.04E-10	7.81E-11	7.81E-11	5.18E-11
Eu-155	6.20E-11	1.40E-10	2.45E-11	1.83E-11	1.83E-11	1.22E-11
Na-22	1.65E-10	3.72E-10	6.52E-11	4.88E-11	4.88E-11	3.24E-11
Ba-133	1.05E-10	2.37E-10	4.16E-11	3.11E-11	3.11E-11	2.06E-11
Mn-54	8.53E-11	1.93E-10	3.37E-11	2.52E-11	2.52E-11	1.67E-11

Table 5-6. Matrix property γ [m/sqrt(s)] calculated for different tracers and different geological material. All tracers show a trend of decreasing γ from the fracture towards the inner parts of the matrix.

	Fracture coating (d_{coat})	Fault gouge (d_{goug}, concept A)	Cataclasite /Mylonite (d_{cata}, 20%)	Altered zone (d_{alt}, #19 hydro Alt. 80%)	Altered zone (d_{alt}, BG1)	Intact wall rock (d_{rock})
Uranine	3.94E-07	2.37E-06	4.95E-08	2.57E-08	2.57E-08	1.05E-08
Amino G	3.94E-07	2.37E-06	4.95E-08	2.57E-08	2.57E-08	1.05E-08
I	7.87E-07	4.73E-06	9.90E-08	5.14E-08	5.14E-08	2.09E-08
Tb-160	3.94E-07	2.37E-06	4.95E-08	2.57E-08	2.57E-08	1.05E-08
Sr	1.74E-06	8.02E-06	3.80E-07	1.13E-07	1.13E-07	8.24E-08
Rb	1.28E-05	2.59E-05	3.23E-06	6.86E-07	6.86E-07	6.25E-07
Cs	4.05E-04	9.81E-04	8.83E-05	7.67E-06	7.67E-06	6.25E-06
HTO	8.13E-07	4.88E-06	1.02E-07	5.30E-08	5.30E-08	2.16E-08
Eu-155	3.94E-07	2.37E-06	4.95E-08	2.57E-08	2.57E-08	1.05E-08
Na-22	2.12E-06	5.65E-06	1.58E-07	1.11E-07	5.51E-08	4.56E-08
Ba-133	1.88E-05	3.73E-05	1.18E-06	9.32E-07	5.78E-07	3.76E-07
Mn-54	4.23E-05	8.38E-05	2.66E-06	2.10E-06	1.30E-06	8.45E-07

5.3 Model fitting using CPT-4C pre-test results

CPT-4C breakthrough curves have been calculated using the BS2B prediction model and parameters. The approach has been to try to keep the micro-structural model as it is defined for is the Type 1 and Type 2 features. Calibration of the model is mainly made by tuning the hydrodynamic control of retention of the flow paths (WL/Q). The order of magnitude of the WL/Q is based on the background flow field as it has been presented in the Section 5.1, i.e. it is about 10^8 s/m for flow path I and $3 \cdot 10^8$ s/m for the flow path II.

During the fitting it became evident that it is not possible to reproduce the CPT-4C results by keeping both the assumption of bulk flow and the given micro-structural model. During the fitting procedure it was therefore decided to retain the bulk flow and change the micro structural model. In the evaluation this decision is revisited and also variable flow is considered, cf. Section 7.

Different ways to alter the micro-structural model were investigated. The only way to improve the performance of the model was to increase the thickness of the fault gouge in the Type 1 features (Structure #19). This was especially true for the Flow path II, which contain both Type 1 and Type 2 features (source in BG1 and sink in Structure #19). In principal, using the selected bulk flow the observed tailing in the breakthrough curves can be reproduced only by a sufficiently thick layer of high porosity material.

The modelling shows that retention time is much longer in the Type 1 feature. Figure 5-5 shows retention by matrix diffusion for a non-sorbing tracer along a Type 1 and Type 2 feature when the WL/Q is kept fixed. Retention in the Type 1 feature is dominated by the fault gouge. The breakthrough curve (red line) indicates that the 0.3 cm thick layer of fault gouge becomes saturated in the applied flow field (the tailing of the breakthrough diminishes, changing the behaviour towards a Gaussian type pulse). Figure 5-5 also shows the case of increased thickness of fault gouge (from 0.3 cm to 3 cm) that has been used in the prediction calculations. In that case fault gouge behaves as an infinite immobile layer during the experimental time scale. For a Type 2 feature the coating also gets saturated and in order to get significant tailing and retention from the altered zones requires unrealistically high values of the WL/Q compared to the rough estimates based on the background flow field.

Based on the modelling of the CPT-4C test the predictions of the BS2B tests with sorbing tracers have been calculated using micro-structural specification given in Table 3-1 and other data in Table 5-3, Table 5-4 and Table 5-5 with an added modification that the thickness of the fault gouge is increased from 0.3 cm to 3 cm. Figure 5-6 and Figure 5-7 show how the increased thickness of the fault gouge affect the breakthrough curves. It seems that fault gouge does not become saturated along the flow path I because the difference between the original and increased thickness of the fault gouge is very small for this flow path. Along flow path II, however, a clear change in the tailing of the breakthrough curve takes place. It is also noted that because the Type 2 feature does not have a significant influence on the retention along the flow path II, the predictions are calculated using only the Type 1 part of the flow path.

One application of the CPT-4C modelling results is that, in addition to the fine tuning of the retention model, it has also been used to estimate the advective delay along both flow paths. The CPT-4C modelling indicates 6 hour advective delay along flow path I (source and sink in Structure #19) and 120 hours advective delay for flow path II (source in BG1 and sink in Structure #19). These same advective delays have been applied in the BS2B prediction, although the pumping rate has been slightly lowered in the BS2B tests (about 2.5 l/min instead of the 2.8 l/min used in CPT-4C).

As a conclusion the parameters used in the prediction calculations are compiled in Table 5-7.

Table 5-7. Overview of data used in predictions.

Parameter	Value (source)
Sorption properties (Kd values)	Table 5-3
Pore diffusivities	Table 5-5
Micro-structural model of the immobile pore space	Table 3-1 and Figure 3-4 (data delivery No. 4), except that thickness of the fault gouge is increased from 0.3 cm to 3 cm
Pumping rate at sink (KI0025F03:R3)	2.45 l/min (based on Andersson et al., 2005)
WL/Q for flow path I (source and sink in Structure #19)	1.59 y/m ($5 \cdot 10^7$ s/m)
WL/Q for flow path II (source in BG1 and sink in Structure #19)	11.1 y/m ($3.5 \cdot 10^8$ s/m)

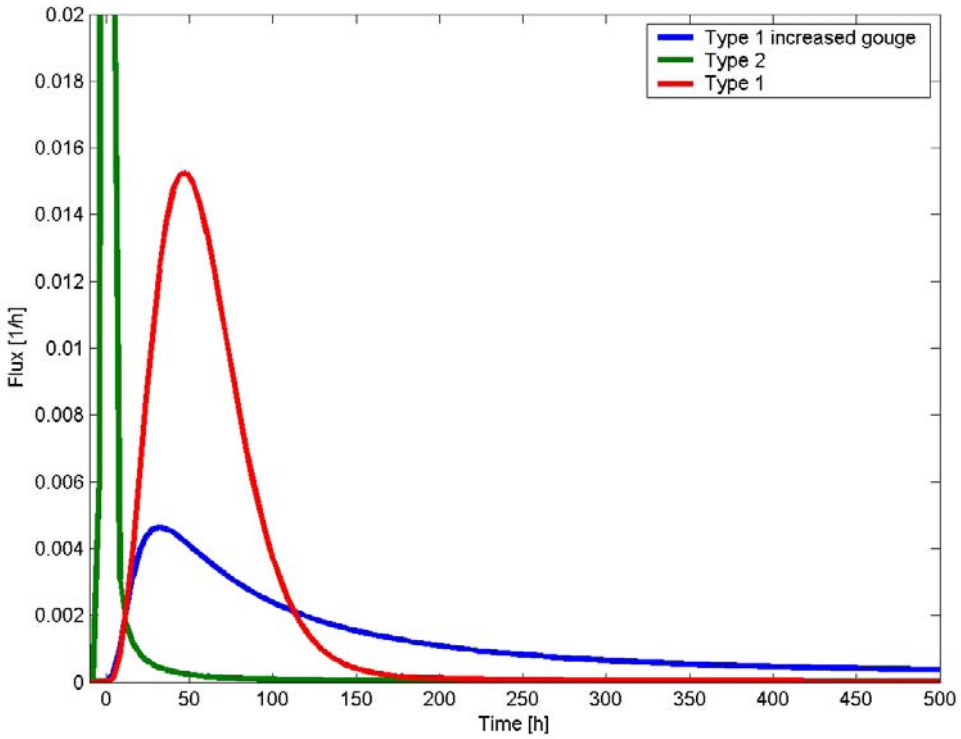

Figure 5-5. *Retention by matrix diffusion for a non-sorbing tracer along Type 1 and Type 2 features using the WL/Q=$3.5 \cdot 10^8$ s/m for all cases (this the WL/Q used for the flow path II in the prediction calculations). Type 1 with increased thickness of fault gouge (blue line) has been used in the predictions.*

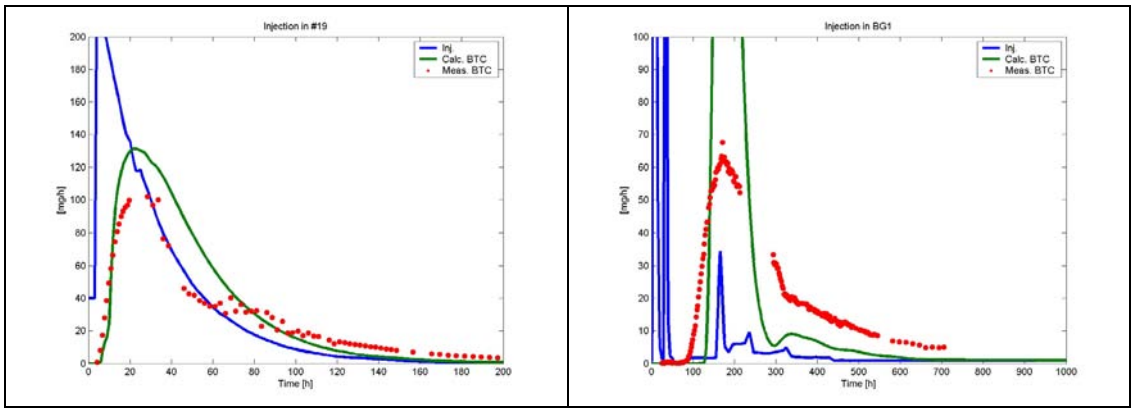

Figure 5-6. *Measured (dots) and calculated breakthrough curves (green lines) for the CPT-4C test. In this case the given BS2B micro-structural model of the Type 1 and Type 2 features has been applied. The injection source term is presented by the blue line. Path I (left) and Path II (right).*

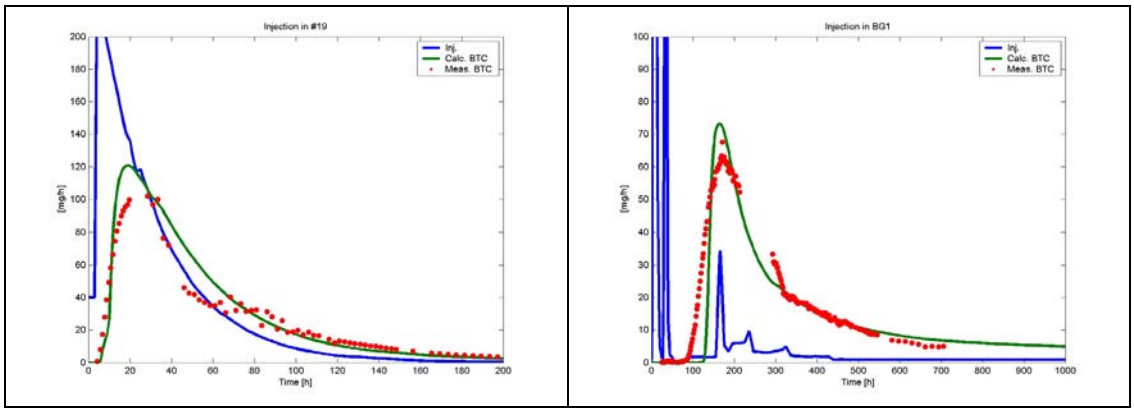

Figure 5-7. *Measured (dots) and calculated breakthrough curves (green lines) for the CPT-4C test. In this case the thickness of the fault gouge has been extended from 0.3 cm to 3 cm. The injection source term is presented by the blue line. Path I (left) and Path II (right).*

6 Model predictions and comparison with BS2B results

BS2B predictions show that a bulk flow field is not able to reproduce the observed behaviour at the early breakthrough times. The early breakthrough could be governed more by the advective field. This means that the flow field characterises the early breakthrough and the importance of the interaction with immobile pore space in that part of the breakthrough curve is not that important for the evaluation of retention processes.

The measured and predicted breakthrough curves show larger difference for the more sorbing tracers. This is partly due to the same reason as for the non-sorbing tracers, i.e. that the variable flow may have dominated the early breakthrough and it cannot be described by the averaged bulk flow. The recoveries of the sorbing tracers are clearly smaller than for the non-sorbing tracers that may emphasize this difference.

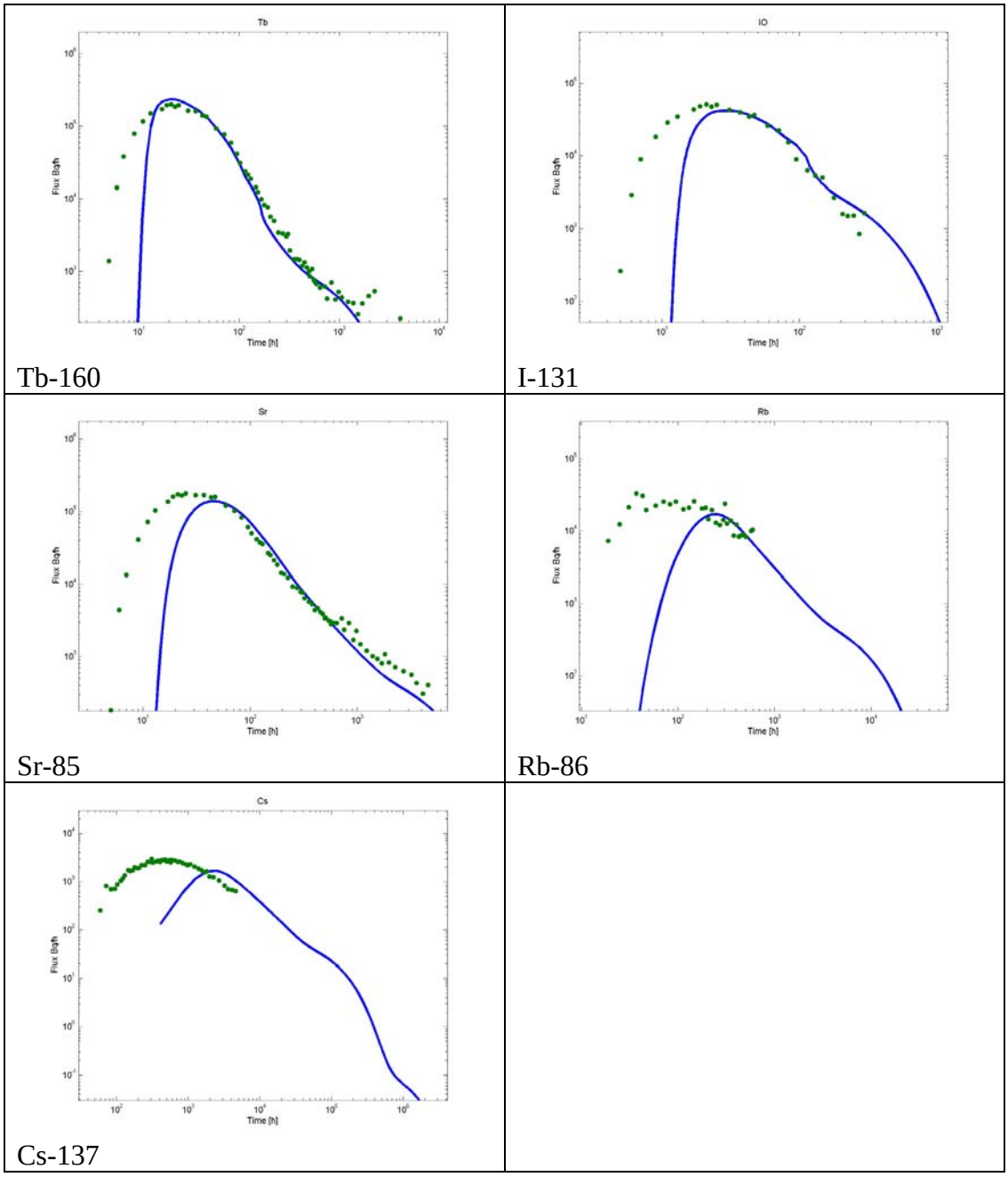

Figure 6-1. *Measured and predicted breakthrough curves for flow path I (source and sink in Structure #19). Measured values are presented as dots and predicted results using solid lines. Note that the breakthrough curves are presented in loglog-scale.*

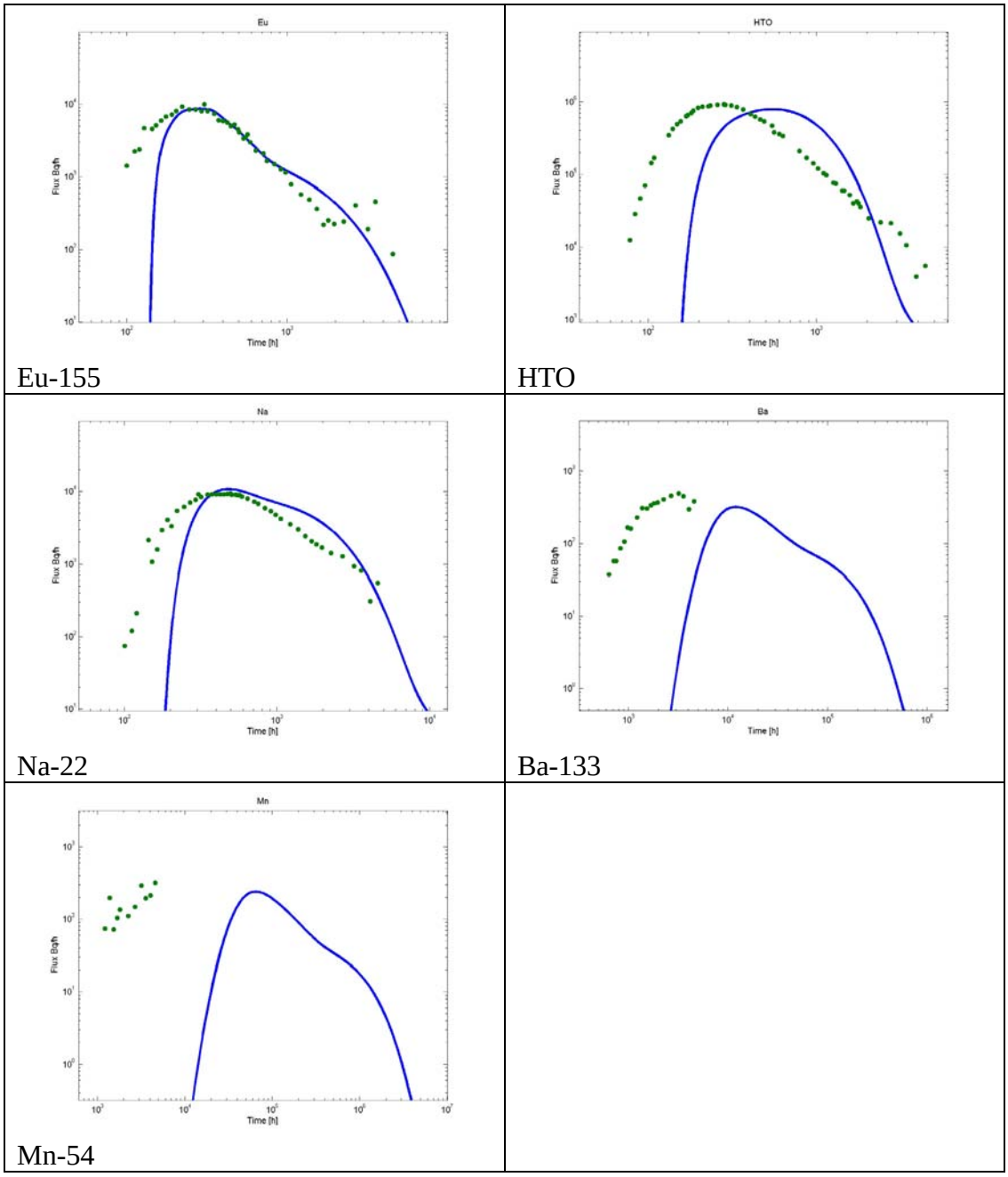

Figure 6-2. *Measured and predicted breakthrough curves for flow path II (source in BG1 and sink in Structure #19). Measured values are presented as dots and predicted results using solid lines. Note that the breakthrough curves are presented in loglog-scale.*

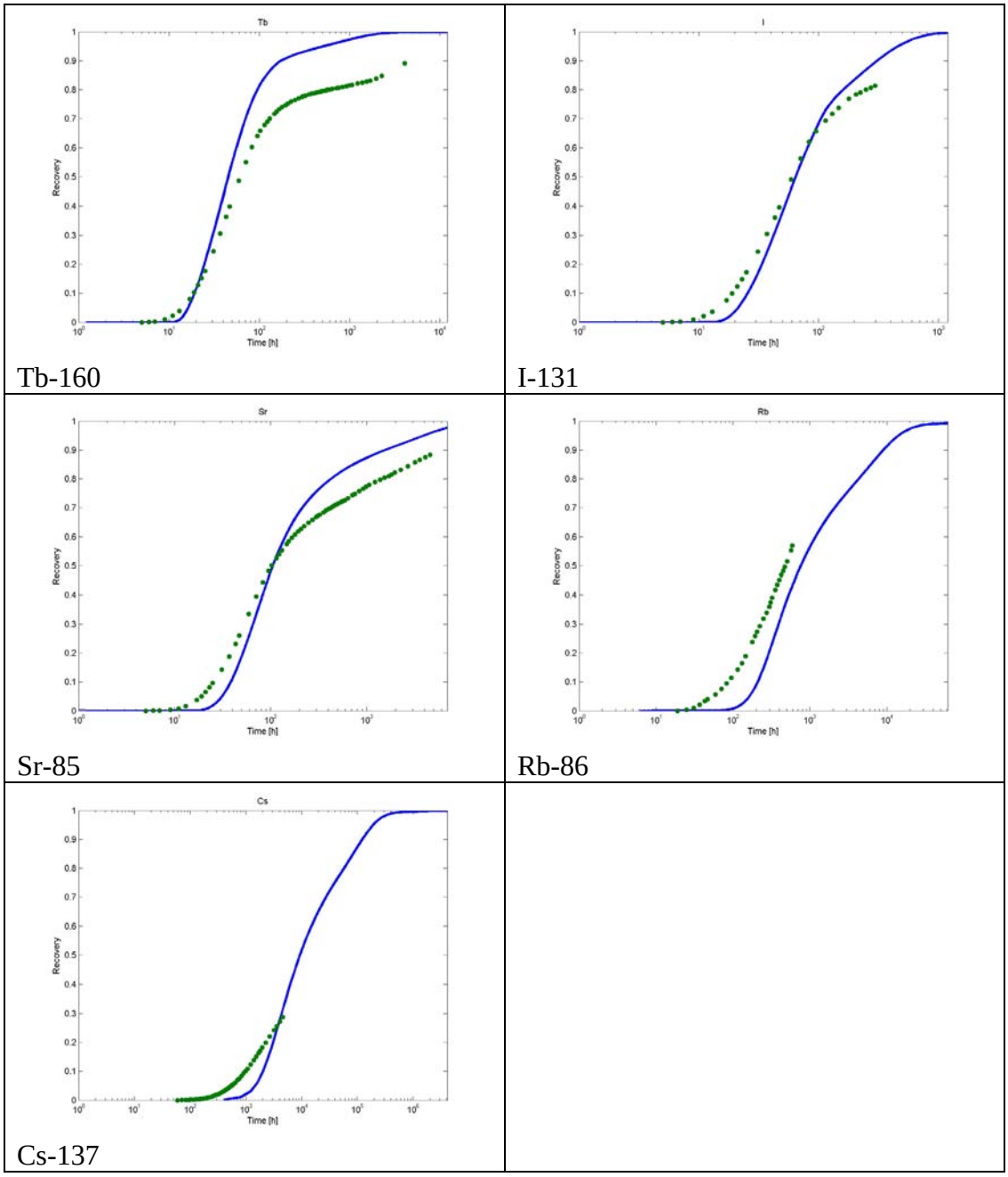

Figure 6-3. *Measured and predicted recovery curves for flow path I (source and sink in Structure #19). Measured values are presented as dots and predicted results using solid lines. Note that the time scale is logarithmic.*

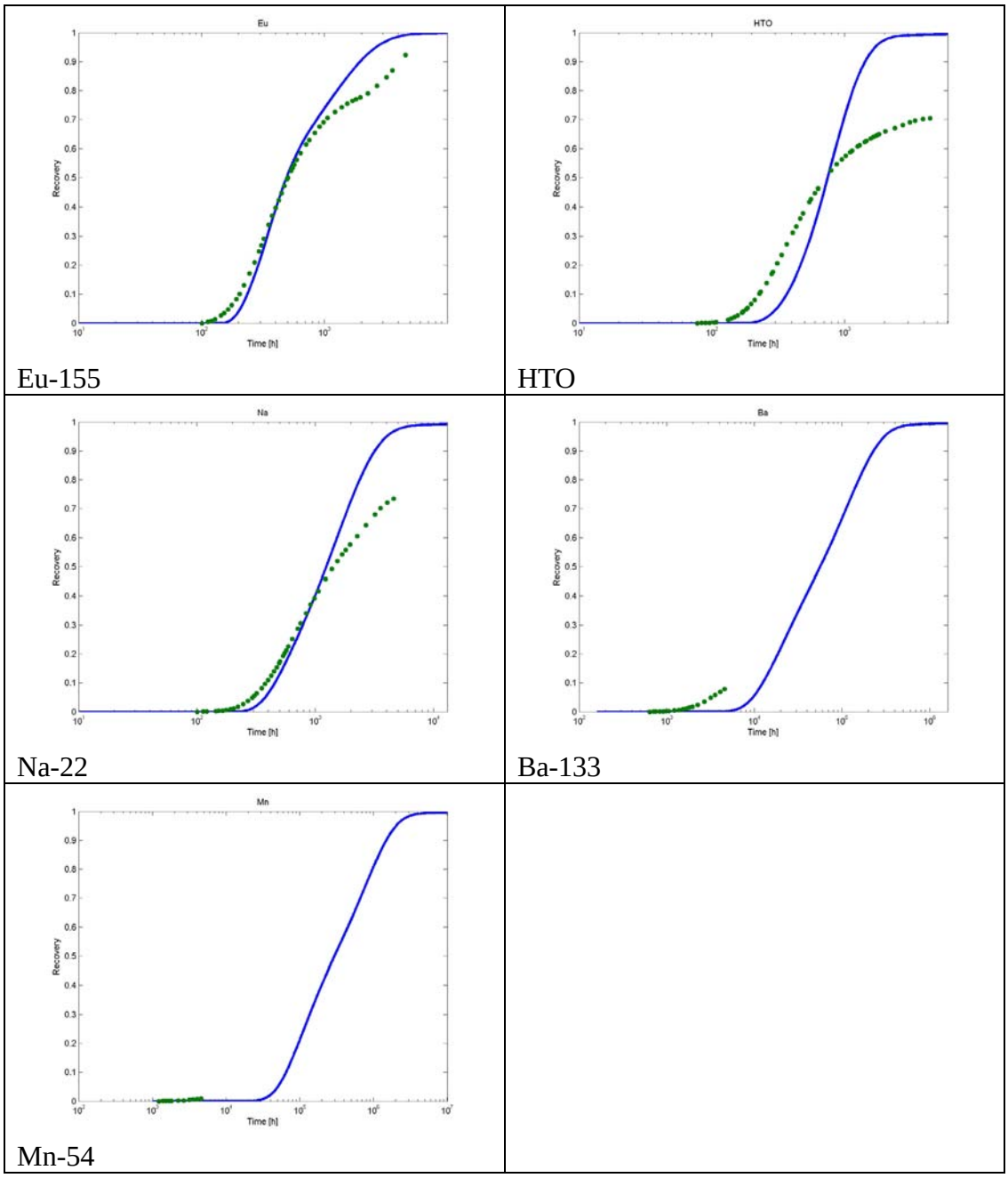

Figure 6-4. *Measured and predicted recovery curves for flow path II (source in BG1 and sink in Structure #19). Measured values are presented as dots and predicted results using solid lines. Note that the time scale is logarithmic.*

7 Evalution

The evaluation does not aim at calibration of the properties of the individual tracers to get the best possible fit between the modelled and measured breakthrough curves. Rather, the approach is to critically bring out the problems and possible contradictions of the different possible explanations. Instead of considering individual tracers, all tracers are studied in parallel to obtain indications of the dynamics of the system.

The same transport model (Section 5.2) as in the prediction phase has been applied in the evaluation, but also the variable flow is taken into account.

7.1 Processes considered in the evaluation

The evaluation concentrates on the few key important processes that are sorption and matrix diffusion. All chemical interactions are represented through linear and equilibrium sorption that is described by the K_d-values of the tracers.

Matrix diffusion takes place in the immobile pore space of the geological materials that are next to the flow channel. The immobile pore space is described by the micro-structural model that includes fracture coating, fault gouge, cataclasite, altered wall rock and intact rock. The aim is to test the micro-structural model that is defined in Figure 3-4 and Table 3-1.

Three cases have been modelled: all geological layers included as given in the definition of the micro-structural model, all layers but with changed properties for fault gouge, and only altered zone and intact rock taken into account. Retention of the tracers depends both on flow field and micro-structural model of the pore space. This means that the variants of the micro-structural should also reflect corresponding differences in the flow field. The basis of the current evaluation is to try to consider how realistic the different variants are and what problems they may entail.

Variability in the flow field is taken into account by a robust model of hydrodynamic dispersion represented using a Gaussian distribution of the advective residence times. It is not possible to directly fit the advective flow field, if we believe that the interactions (matrix diffusion) also have an important role in the breakthrough (curves) of the non-sorbing tracers. For this reason the advective field is fitted jointly together with the hydrodynamic control of the flow (WL/Q).

It may also be possible that other processes than matrix diffusion and linear equilibrium sorption have been important during the tracer transport. For this reason, different tracers are considered in the next section to judge how reliable information they can provide for the evaluation process.

7.2 Behaviour of the different tracers

The tracers used for the BS2B sorbing experiment span a range of diffusivities and sorption properties. This is essential for the evaluation, but an inevitable consequence of the application of the sorbing tracers is that the recovery of the most sorbing tracers can be quite low at the termination time of the experiment. This is especially true for the flow path II (injection in the background fracture BG1) where the recovery of both Mn-54 and Ba-133 is less than 10%. Recovery of the Mn-54 is in fact only a couple of percent.

Meaningful evaluation also requires that the source term of the tracer is well defined and that the breakthrough curve reflects process taking place during the transport through the fracture. To investigate this part of the problem the source terms of the different tracers are plotted in Figures 7-1 to 7-3. For a flow path II (Figure 7-3) all source terms show consistent behaviour of a well-mixed source volume that is diluted by the injection flow rate. Along flow path I only Ba-133 shows slight deviation of this behaviour. For flow path I there seems to be some problems with the Cs-137. The source term of Cs-137 (Figure 7-1 and Figure 7-2) does not at all follow the typical dilution curve of the other tracers. It even shows matrix diffusion type behaviour of $t^{-3/2}$ tailing (Figure 7-2). To some extent similar type of behaviour can be seen in the source term of the Rb-86. Similar behaviour of the Cs (and also Rb) has been observed already in the TRUE Block Scale experiment. Andersson et al. (2002) note that it is possible to explain the power-law behaviour of the Cs in the injection curves by applying non-linear sorption with Freundlich isotherm.

As a summary, it can be concluded that evaluation cannot rely very much on the very low recovery tracers Mn-54 and Ba-133. We also need to be cautious with the Cs-137, and possible also Rb-86, responses, because their behaviour may include more complicated (chemical) processes that cause their injection curves to deviate from the dilution curve.

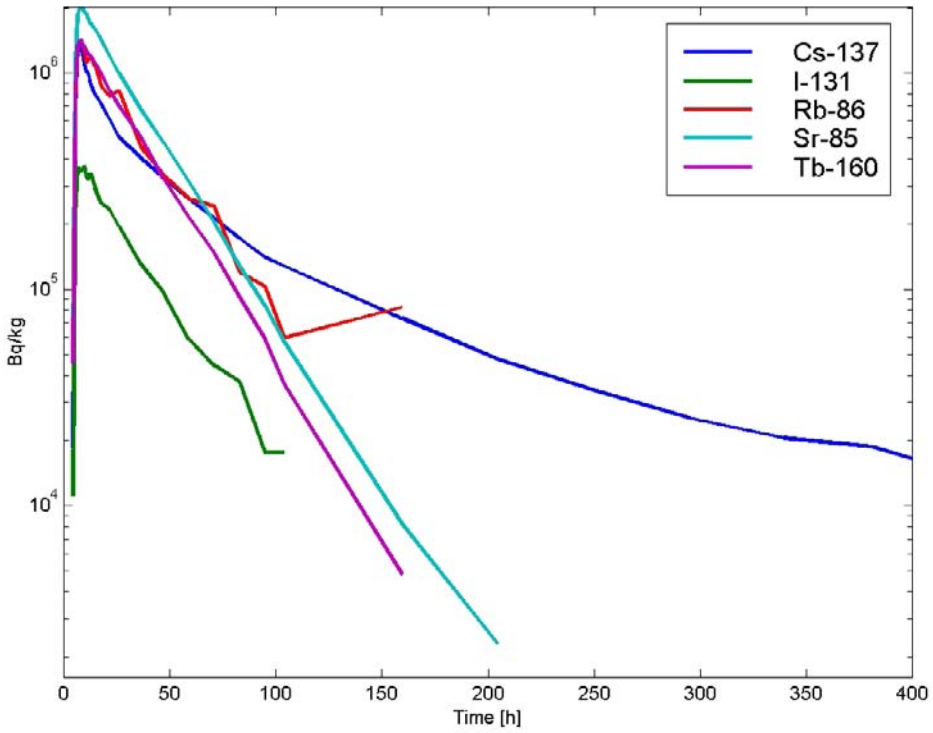

Figure 7-1. *Measured source terms of tracers used in flow path I (injection in Structure #19) plotted on lin-log scale.*

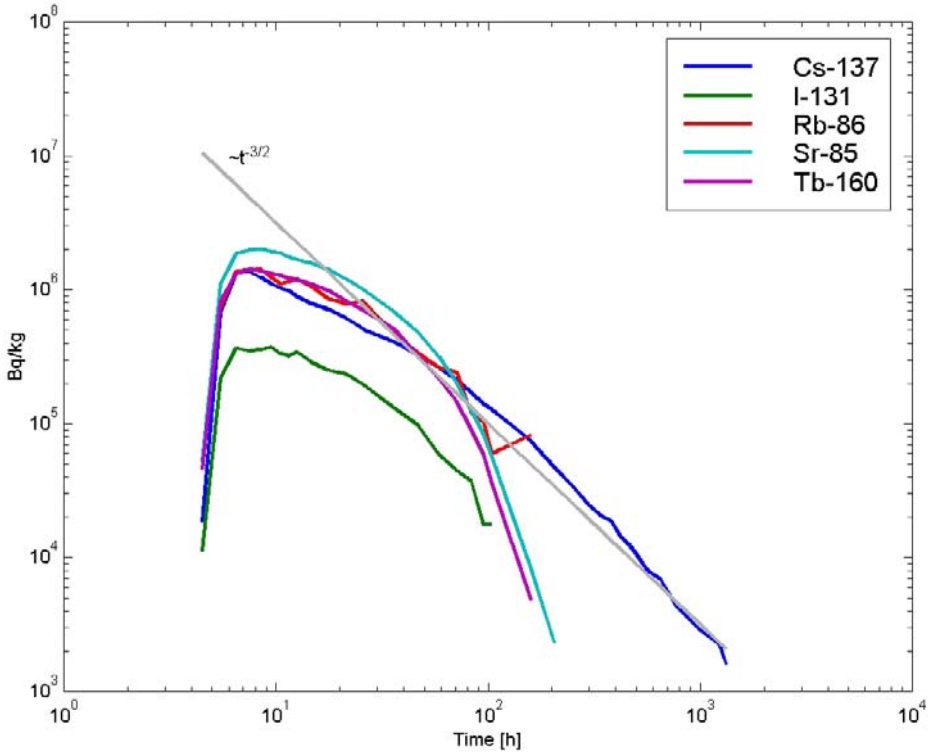

Figure 7-2. *Measured source terms of tracers used in flow path I (injection in Structure #19) plotted on log-log scale.*

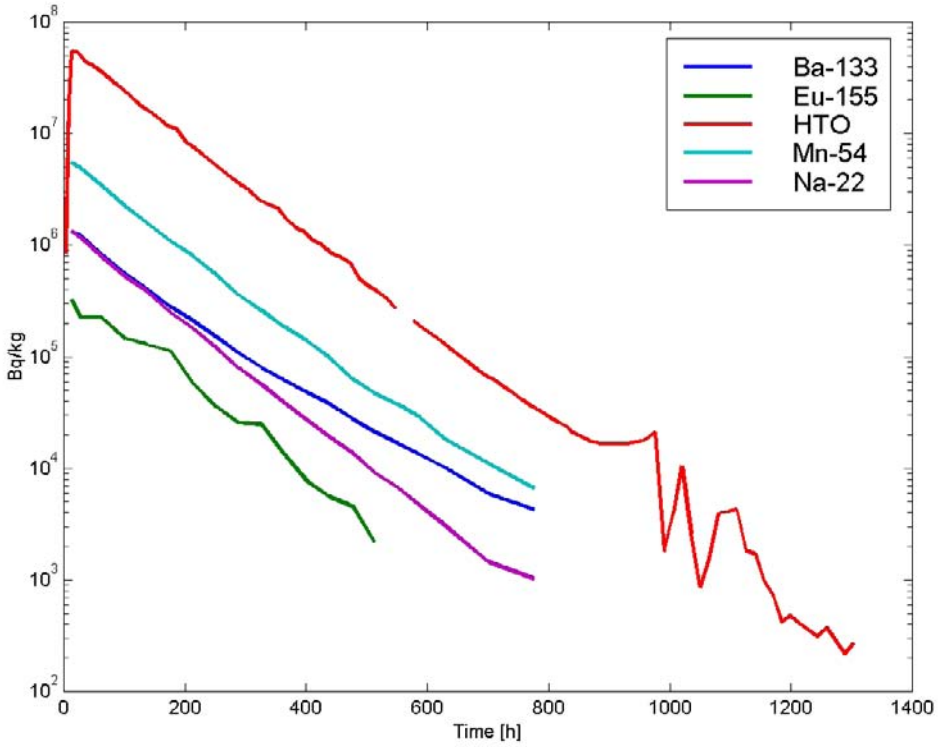

Figure 7-3. *Measured source terms of tracers used in flow path II (injection in the background fracture BG1) plotted on log-log scale.*

7.3 Response functions of the different tracers

A first way to study the tracer breakthrough curves is to try to deconvolute the source term from the breakthrough curves. In principal, this should give the response function of the flow path that is characterised only by the transport and retention processes. Figures 7-4 and 7-5 show the deconvoluted response functions and also the calculated breakthrough curves using the deconvoluted response functions. The deconvolutions have been made for the non-sorbing tracers that have the lowest diffusivity. These tracers are least sensitive to retention by matrix diffusion, however, along both flow paths the tailings of the response functions show $t^{-3/2}$ behaviour. The latter is typical for unlimited matrix diffusion and we may also note that neither of the response functions show indications of limitation in the accessible volume of the immobile pore space. In both cases the deconvolution is performed using Tikhonov regularised inversion of the discretized convolution equations.

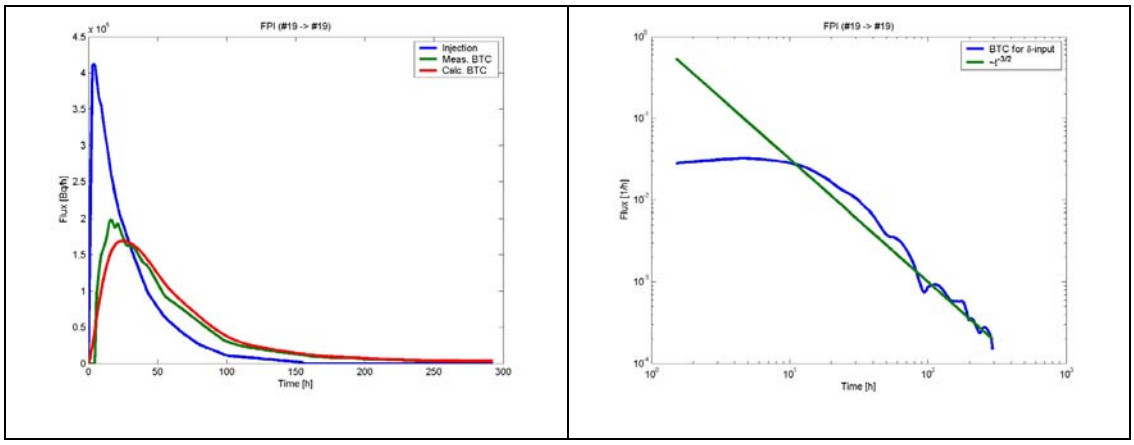

Figure 7-4. *Deconvolution of the Tb-160 breakthrough curve for flow path I (injection in Structure #19). The right figure shows the deconvoluted response function and the left figure shows the measured injection and breakthrough curves (blue and green) together with the breakthrough curve calculated using the deconvoluted response function (red).*

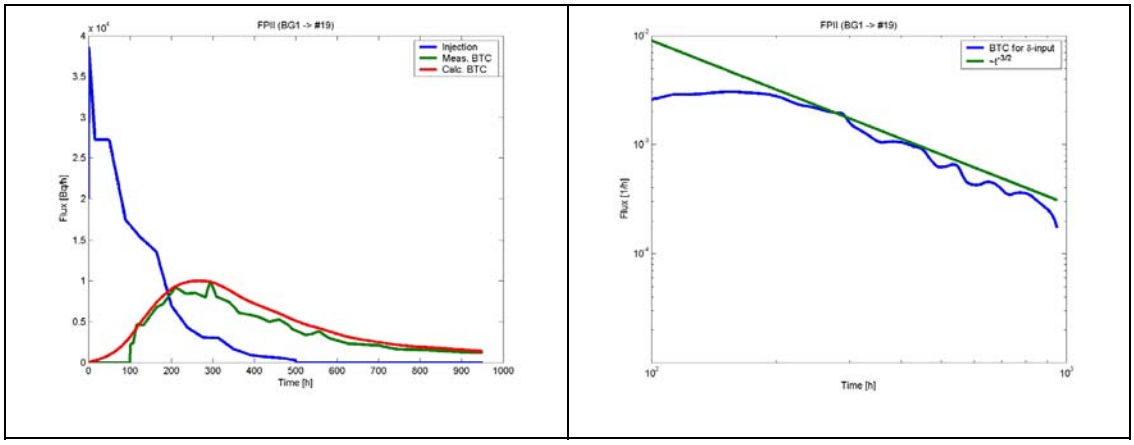

Figure 7-5. *Deconvolution of the Eu-155 breakthrough curve for flow path II (injection in background fracture BG1). The right figure shows the deconvoluted response function and the left figure shows the measured injection and breakthrough curves (blue and green) together with the breakthrough curve calculated using the deconvoluted response function (red).*

It may also be noted that using the solution of the matrix diffusion equation for the delta-input as a response function gives good fits with the measured breakthrough curves. The procedure is that the response function is defined by the matrix diffusion breakthrough curve for the δ-function release

$$f(t) = \frac{u}{\sqrt{\pi}}\left(t - t_w\right)^{-3/2} \exp\left(-\frac{u^2}{t - t_w}\right) \quad . \tag{7-5}$$

This function is convoluted with the tracer source term and the resulting breakthrough curve is fitted to the measured breakthrough curve using u as the fitting parameter. It is possible to carry out this fitting procedure to all other tracers except Cs-137 (flow path I), where both retardation and spreading of the breakthrough pulse were not reproduced by this model, and low recovery tracers Ba-133 and Mn-54 (flow path II). The resulting calculated breakthrough curves with the corresponding measured breakthrough curves are presented in Figure 7-6 and Figure 7-7. Fitted parameters are presented in Table 7-1.

It is also possible to calculate the corresponding u-values for the different layers of the micro-structural model (i.e. coating, fault gouge, cataclasite, altered zones and intact rock) using equation (7-6).

$$u = \varepsilon\sqrt{D_p R_p}\,\frac{WL}{Q} \quad , \tag{7-6}$$

where ε is porosity, D_p is pore diffusivity, R_p is retardation factor and $WL/Q=t_w/2b$ defines the flow field where W is width of the transport channel, L is the length of the flow channel, Q is the flow rate, t_w is the water residence time and $2b$ is the transport aperture. Two alternatives for WL/Q are applied; other parameters form the matrix parameter group γ, which has already been calculated for different layers in Table 5-6.

The first WL/Q applied in this comparison was the one used in the predictions and it is based on the considerations of the measured (dilution) flow rates at the injection sections and calibration using CPT-4C (see Section 5.1 and Table 5-7). In this case $WL/Q=5\cdot10^{7}$ s/m for the tracers along the flow path I (injection in #19) and $WL/Q=3.5\cdot10^{8}$ s/m for the flow path II (injection in BG1). The second alternative is calculated using a 40 times higher WL/Q along both flow paths.

Figures 7-6 and 7-7 show the comparison between calculated and fitted parameter u-values for both selected flow fields. Fitted u-values (Table 7-1) are shown by red pentagrams and calculated u's for the different geological materials are shown by different markers. An overall conclusion is that the calculated parameter values follow the same trend amongst different tracers as the experimental results (i.e. the fitted deconvolution curve). Figures 7-6 and 7-7 also show that the background flow can explain the measured breakthrough curves if the material properties are close to those of the fault gouge. If the material properties of the immobile pore space are close to that of the altered zone, then a 40 times larger WL/Q is required (Figure 7-9).

We should note that the robust comparisons in Figures 7-8 and 7-9 treat all immobile zones as if they were infinite. Especially, limitation in the extent of the coating and fault gouge may affect the results. However, the charts in Figures 7-8 and 7-9 show the potential retention power that the different geological materials have and they also exemplify how large changes in the flow field that are required to change principal retention zone properties from e.g. a pure effect of fault gouge to a pure effect of altered zone.

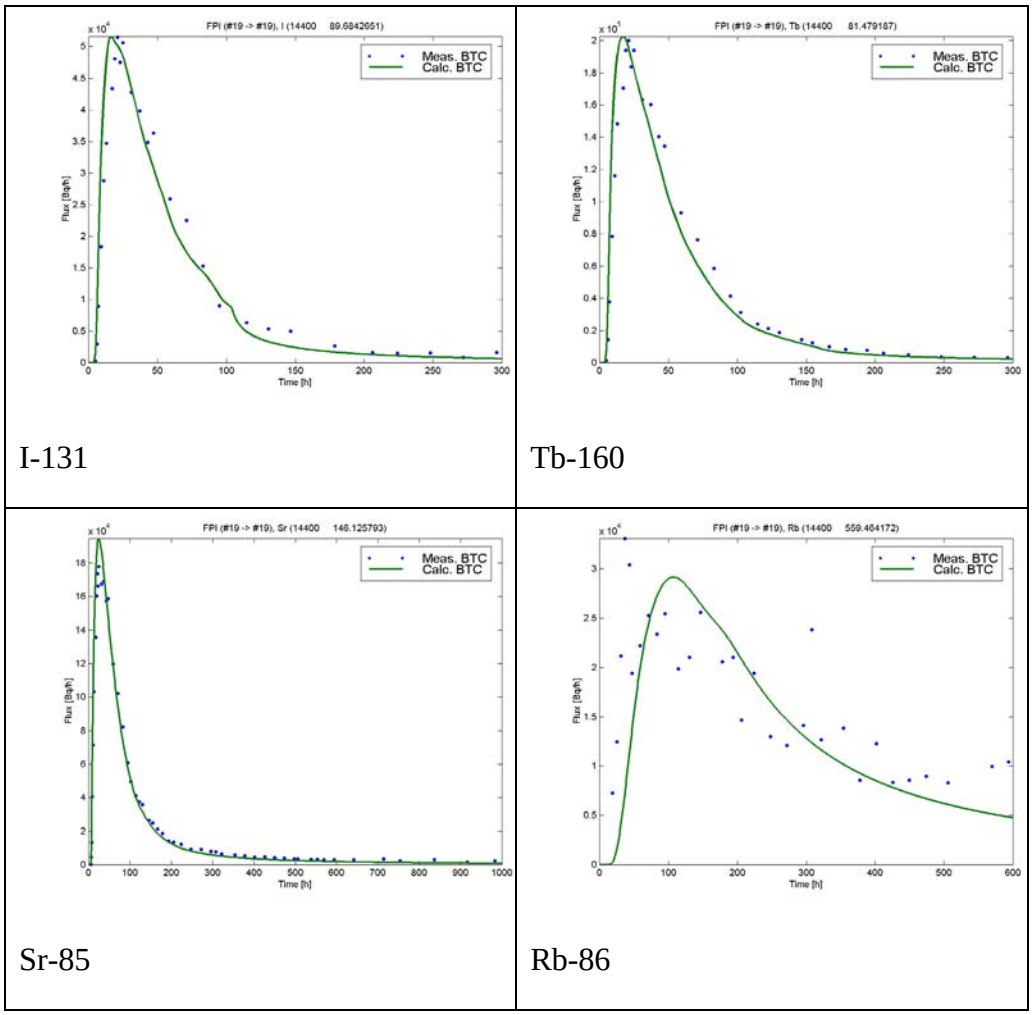

Figure 7-6. *Measured (dots) and fitted breakthrough curves for the tracers of the flow path I (injection in #19). Fitted flow paths are calculated by restricting the tracer response function to matrix diffusion breakthrough curve for δ-function input (equation (7-5)) and fitting the parameter u. Fitted u-values are given in Table 7-1.*

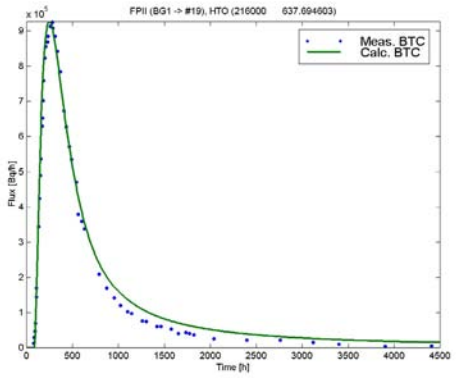

HTO

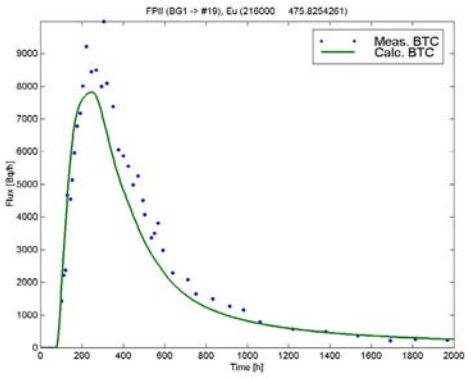

Eu-155

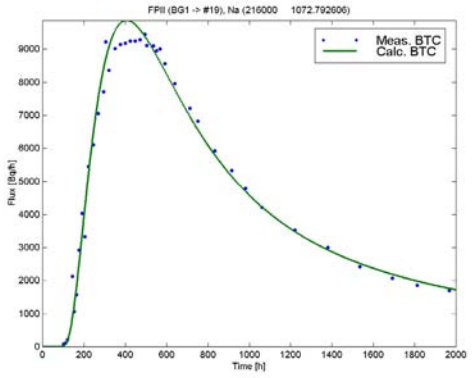

Na-22

Figure 7-7. *Measured (dots) and fitted breakthrough curves for the tracers of the flow path II (injection in BG1). Fitted flow paths are calculated by restricting the tracer response function to matrix diffusion breakthrough curve for δ-function input (equation (7-5)) and fitting the parameter u. Fitted u-values are given in Table 7-1.*

Table 7-1. Parameters of the fitted matrix diffusion response functions (equation (7-5)) for the different tracers.

Tracer	***u* [sqrt(h)]**	**t_w [h]**
I-131 (Flow Path I)	1.5	4
Tb-160 (Flow Path I)	1.4	4
Sr-85 (Flow Path I)	2.4	4
Rb-86 (Flow Path I)	9.3	4
HTO (Flow Path II)	11	60
Eu-155 (Flow Path II)	7.9	60
Na-22 (Flow Path II)	18	60

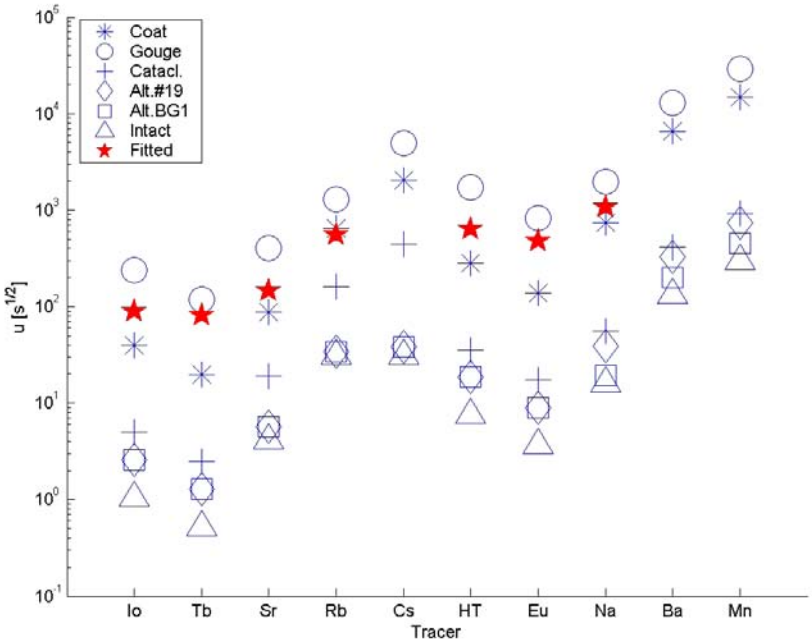

Figure 7-8. *Parameter u-values (7-6) calculated for different tracers. The u-values are calculated using material properties (γ) from Table* 5-6 *and assuming a flow field that is characterised by the pumping of the borehole sections and the background flow fields (WL/Q=5·10^7 s/m for the tracers along the flow path I and WL/Q=3.5·10^8 s/m for the tracers along the flow path II, see Section 5.1 and Table* 5-7*). Fitted parameter u-values (Table 7-1) are indicated by red pentagrams.*

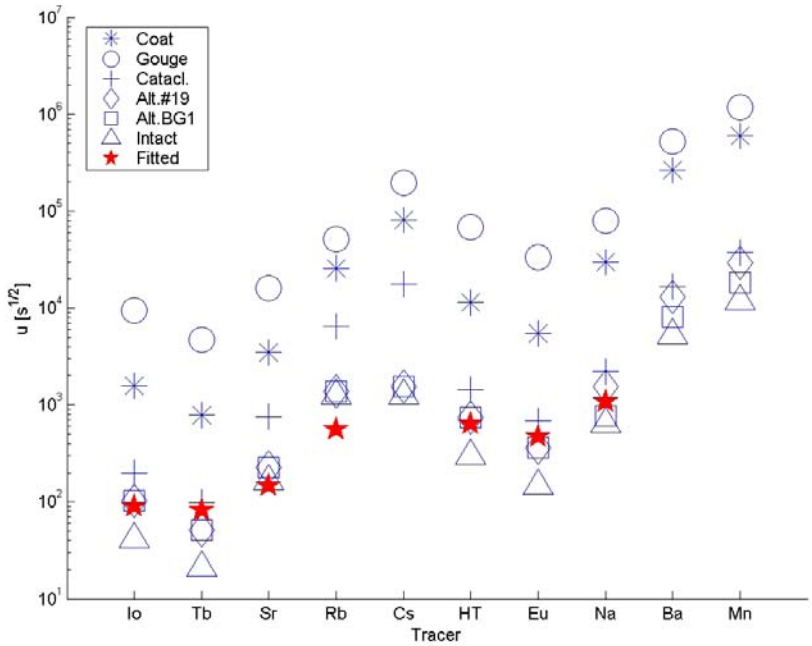

Figure 7-9. *Parameter u-values (7-6) calculated for different tracers. The u-values are calculated using material properties (γ) from Table* 5-6 *and assuming a flow field that is characterised by 40 times larger WL/Q as for Figure 7-8 (WL/Q=200·107 s/m for the tracers along the flow path I and WL/Q=140·108 s/m for the tracers along the flow path II, see Section 5.1 and Table* 5-7*). Fitted parameter u-values (Table 7-1) are indicated by red pentagrams.*

7.4 Flow field and hydrodynamic control of retention

It is not possible to obtain direct information on the water residence time distribution along the tested flow paths. Non-sorbing and least diffusive tracers show characteristics of the matrix diffusion in the deconvoluted response functions. This indicates that it is likely that all breakthrough curves are affected by retention caused by matrix diffusion type of processes.

Predictions were made using a very simple model that are represented by an average flow rate in the transport calculations. In the evaluation, variable flow is taken into account. Again, a quite simple model is applied and water residence time distributions of the two flow paths are represented by Gaussian distributions. Estimation of the *WL*/*Q*-distribution is based on the Gaussian water residence time distributions. This is done by multiplying the water residence time distribution by a constant factor so that the resulting average *WL*/*Q* of the *WL*/*Q*-distribution is a given value. In practice, this can be interpreted so that the transport channel has a constant aperture and variable flow rate. The multiplying factor that is used to convert the water residence time distribution to a *WL*/*Q*-distribution is the inverse of the effective retention aperture of the transport channel, indicating the equality $WL/Q=t_w/2b$.

Three different cases have been calculated in the evaluation:

A. Original BS2B micro-structural model coupled with a flow field that has average WL/Q based on the measured flow rates at the injection locations (from CPT-3C test)

B. Same flow field as in case A, but increased thickness of fault gouge

C. Only altered rock and intact rock taken into account and increased WL/Q.

The same water residence time distribution has been applied for each flow path in all cases. The applied water residence time distributions are presented in Figure 7-10. The WL/Q-distributions are calculated by dividing the water residence time distribution by the effective retention aperture. The effective retention aperture for cases A and B is about $1.5\cdot10^{-4}$ m for flow path I and about $4.5\cdot10^{-4}$ m for flow path II. In case C the aperture is about $4\cdot10^{-6}$ m for flow path I and $3\cdot10^{-5}$ m for flow path II (i.e. compared to cases A and B the average WL/Q is 40 larger for the flow path I and 15 times larger for flow path II). The water residence time distribution that has been applied for all calculated cases was selected by fitting of the case B breakthrough curves.

The selection of the calculated variants in the evaluation is mainly guided by the information that has been analysed from the measured breakthrough curves in Section 7.3 and presented in Figures 7-8 and 7-9.

Case A is regarded as a base case that uses the given micro-structural model and flow measurements. However, in the evaluation the flow field part has been partly calibrated to average values of $WL/Q=5\cdot10^7$ s/m for flow path I and $WL/Q=8\cdot10^8$ s/m for flow path II. The local flow rate measurements of the CPT-3C test indicated $WL/Q=10^8$ s/m for flow path I and $WL/Q=3\cdot10^8$ s/m for flow path II. Flow path II is composed of Type 1 (#19) and Type 2 (BG1) features. The estimated *WL*/*Q* values given in the Section 5.1 also suggest that the total *WL*/*Q* is divided so that 1/3 of the *WL*/*Q* is along Type 1 and 2/3 along Type 2. This ratio is maintained during the evaluation. Note, that in the predictions the flow path II is completely along Type 1 feature. The reason is that in the prediction model (i.e., WL/Q-values and micro-structural model applied) the Type 1 features completely dominated the retention. Therefore, dropping Type 2 fractures from the simulations did not affect the retention, but sped up calculations.

Case B is a variant that leans towards the effective material properties of the fault gouge as suggested by Figure 7-8. Case C is a variant that is based on the observed unlimited nature of the matrix diffusion (e.g. Figure 7-4 and Figure 7-5). This requirement is fulfilled by the altered zone, but this approach also requires elimination of the fracture coating, fault gouge and cataclasite from the micro-structural model and enhancement of the *WL*/*Q*.

It is also possible to give geometrical interpretation of the transport channels that are based on the average values of the *WL*/*Q*-distributions. Approximate lengths of the flow paths and the injection flow rates of the BS2B experiment are 20 m and 5 ml/min for flow path I and 40 m and 2 ml/min for flow path II, respectively. The average widths of the flow paths are calculated to be about 21 cm for flow path I and 67 cm for flow path II (WL/Q=$5\cdot10^7$ s/m for path I and WL/Q=$8\cdot10^8$ s/m for path II). A variation of the flow field is also calculated where the average WL/Q is 15 to 40 times larger. In this case the geometrical interpretation gives transport path widths that are in the order of 10 m, i.e. almost in the same order of magnitude as the length of the path.

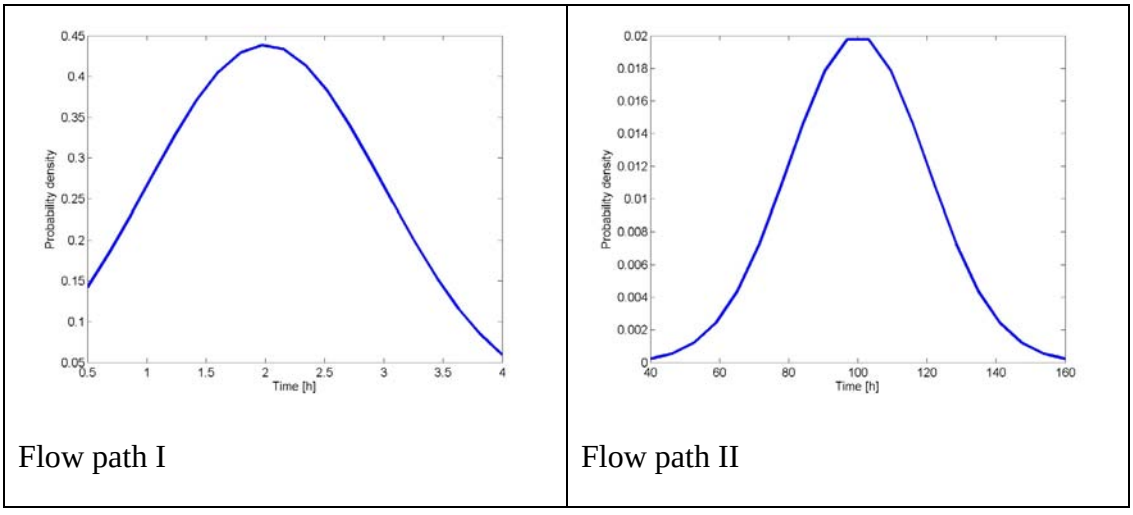

Flow path I | Flow path II

Figure 7-10. *Water residence time distributions that were used in the evaluation of the BS2B experiment.*

7.5 Results for the BS2B micro-structural model

In this case the breakthrough curves are calculated using the basic micro-structural model of the BS2B features (cf. Section 3.1.2) and a flow model that is based on the dilution flow measurements. Parameters used to calculate this case are presented in Table 7-2 and the resulting breakthrough curves are presented in Figure 7-11 and Figure 7-12, respectively. This is the base case of all the evaluation calculations. The two other cases are variations of this case where either the micro-structural model or micro-structural model and flow field are altered.

It can be seen that in this model the retention takes place mainly in the immobile pore space that has a very limited volume. This manifests itself in the results as a more Gaussian type of breakthrough curve. Only a small amount of the tracer mass is in the tailing of the breakthrough curve. Saturation of the fracture coating and fault gouge can also be seen in Figure 7-13, where the contributions of the individual layers to the total breakthrough curve are presented.

The calculated breakthrough curves for the strongly sorbing tracers clearly show later breakthrough than the measured breakthrough curves. Much of the delay of the sorbing tracers is established in the fracture coating. Figure 7-13 shows the calculated contributions of the different immobile layers for a non-sorbing and sorbing tracer along both flow paths. Especially for flow path II (HTO and Mn-54) it can be seen that for Mn-54 the retention caused by fracture coating is as strong as retention caused by fault gouge. For non-sorbing HTO the fault gouge causes much more retention than the fracture coating.

Table 7-2. Specification of the flow field and immobile pore space for the calculation Case A.

Case A	**Immobile zone:** According to the micro-structural model (Table 3-1, Table 5-3 and Table 5-4) **Water residence time distribution:** Flow path I: Gaussian (mean 2.0 h, std 1.0 h) from about -1.5·std to 2·std Flow path II: Gaussian (mean 100 h, std 20 h) from about -3·std to 3·std **WL/Q distribution:** Flow path I: Gaussian (mean $4.8 \cdot 10^7$ s/m, std $2.4 \cdot 10^7$ s/m) from about -1.5·std to 2·std Flow path II: Gaussian (mean $8 \cdot 10^8$ s/m, std $1.6 \cdot 10^8$ s/m) from about -3·std to 3·std, 2/3 of the WL/Q in BG1 and 1/3 in Structure #19

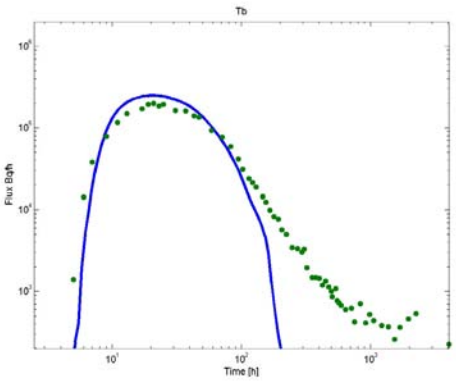

Tb-160

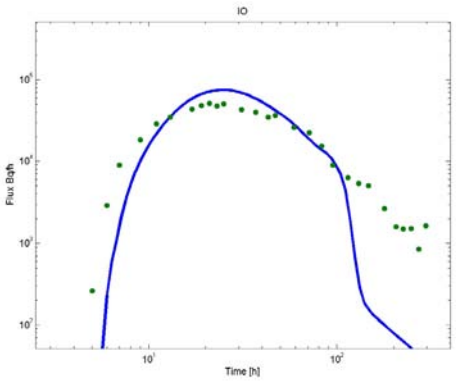

I-131

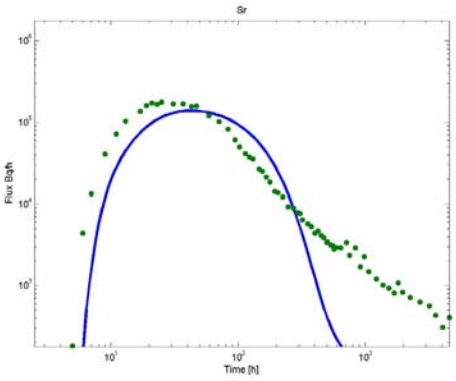

Sr-85

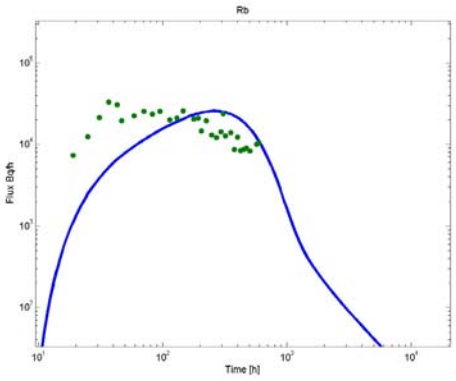

Rb-86

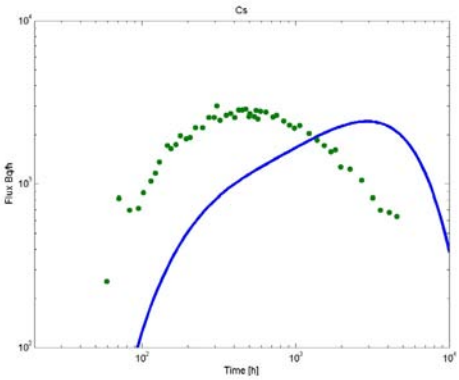

Cs-137

Figure 7-11. *Measured (dots) and calculated breakthrough curves for flow path I. Breakthrough curves were calculated using the BS2B micro-structural model and a flow field as specified in Table 7-2.*

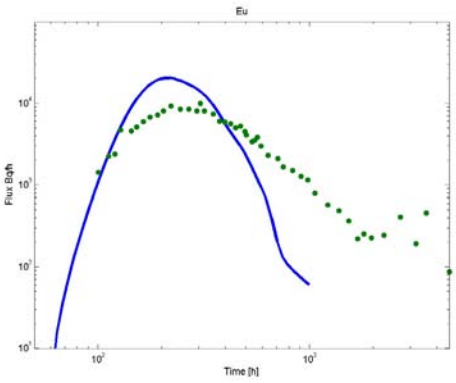

Eu-155

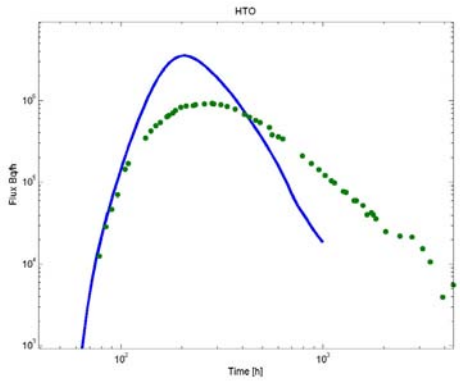

HTO

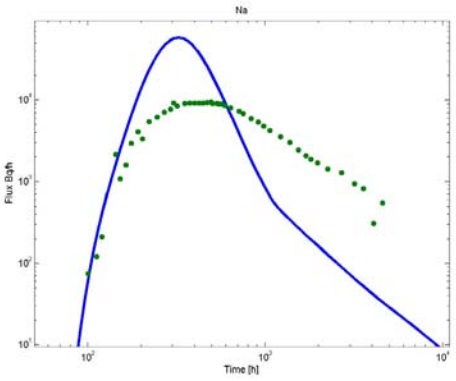

Na-22

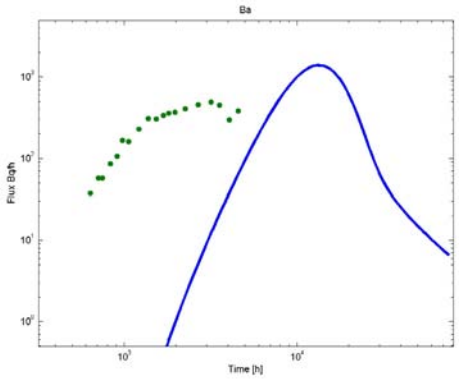

Ba-131

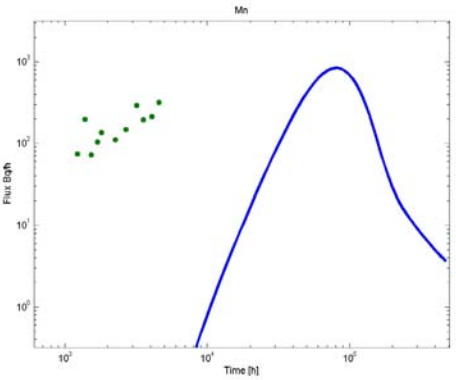

Mn-54

Figure 7-12. *Measured (dots) and calculated breakthrough curves for flow path II. Breakthrough curves were calculated using the BS2B micro-structural model and a flow field as specified in Table 7-2.*

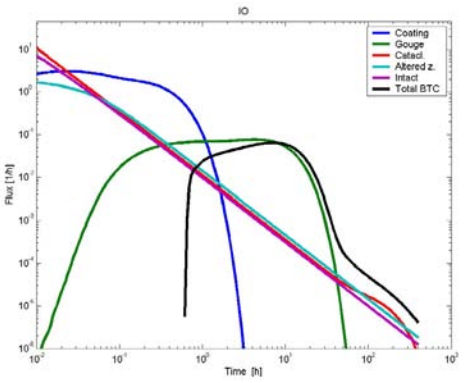

I-131 (path I)

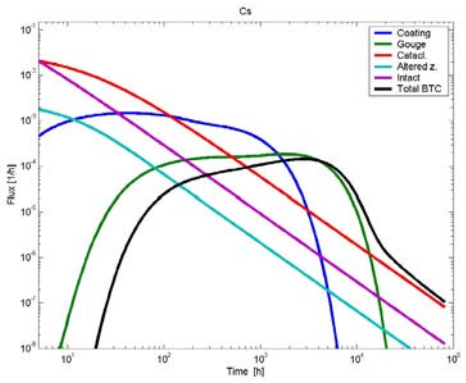

Cs-137 (path I)

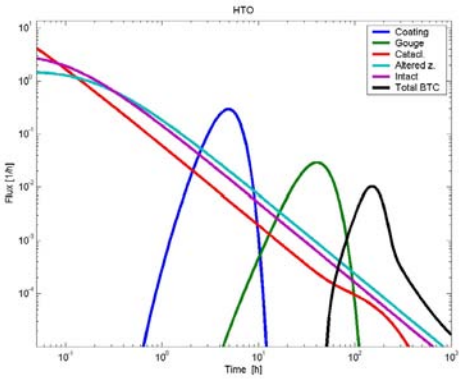

HTO (path II)

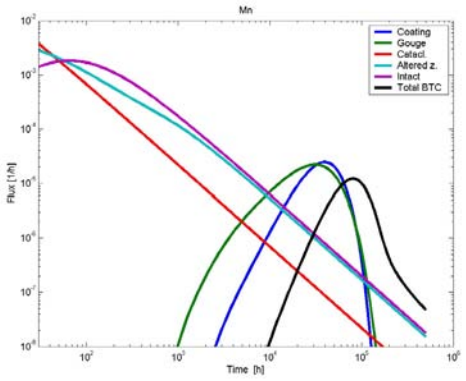

Mn-54 (path II)

Figure 7-13. *Contributions of the different immobile layers to the total breakthrough curve. These curves do not contain advective delay or the injection source term. The total breakthrough (black line) curve is a convolution of the individual contributions presented in these figures. One non-sorbing tracer and one strongly sorbing tracer is selected from both flow paths. It can be observed that especially the delay caused by the fracture coating is more important for sorbing tracers.*

7.6 Results for the case of varied fault gouge

Calculation of this case is motivated by the results presented in Figure 7-8. It suggests that an immobile zone that has properties close to that of fault gouge possibly can explain the breakthrough curves. Another motivation is that in this case it is possible to use the flow field that was measured in the dilution experiment CPT-3C.

The measured breakthrough curves do not show clear signs of limited extent of the major retention zone. Results of the case A (Section 7.5) shows that fault gouge (as defined in the BS2B micro-structural model) will get saturated by the tracers. Especially for the flow path II the modelled breakthrough curves (of case A) are delayed Gaussian pulses that have a minor elements of $t^{-3/2}$ tailing.

Two variants of the BS2B micro-structural model are analysed here. First all layers of the BS2B micro-structural model are taken into account and the thickness of the fault gouge layer is increased from 3 mm to 6 cm. In the second alternative fault gouge thickness is increased and the layer of the fracture coating is removed. The reason to omit the fracture coating is that this thin layer of coating cause delay especially for the more sorbing tracers. It seems that this kind of delay does not exist in the measured breakthrough curves. These two alternative micro-structural models for the Type 1 fractures are presented in Figure 7-14.

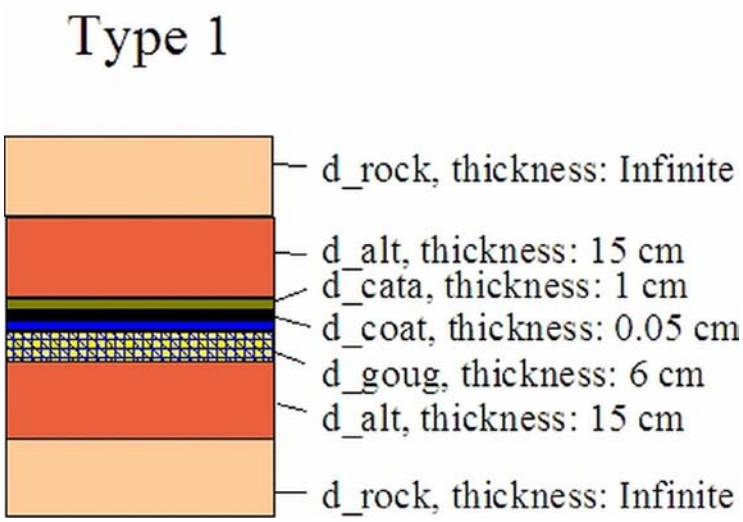

Figure 7-14. *Alternative micro-structural model applied for the Type 1 fractures in the Case B simulations. In the second variant of the Case B the fracture coating was completely removed.*

It may be noted that non-sorbing tracers HTO and Eu-155 show a little bit different behaviour in the modelled breakthrough curves. The limited thickness of the 6 cm fault gouge causes the tailing of the modelled HTO breakthrough curve to rise at around 100 hours, contrary to the measured breakthrough curve. The modelled Eu-155 breakthrough curve does not deviate from the measured breakthrough curve in the same way. The reason for the behaviour of the modelled breakthrough curves is the contrast of the applied pore diffusivities of Eu-155 and HTO. According to the BS2B micro-structural model the HTO diffusivity is over four times larger than Eu-155 diffusivity. In the measured breakthrough curves the contrast in HTO and Eu-155 pore diffusivities seems not to be that large as it is in the BS2B micro-structural model. This is supported by the observation that in the measured breakthrough curves the time of the maximums of the breakthrough curves are quite close to each others. For the unlimited matrix diffusion the maximum of the breakthrough curve (δ-function release) is directly proportional to the pore diffusivity ($\sim u^2$ of equation (7-6)). According to Table 7-1 the difference in u^2 between HTO and Eu-155 is about 1.8, whereas it is over a factor four in BS2B micro-structural model)

Clearly, a vertical 6 cm layer of fault gouge is a problem. It is probably very hard to explain it from a geological point of view.

Table 7-3. Specification of the flow field and immobile pore space for Case B.

Case B	**Immobile zone:** Same as for Case A (Table 7-2), *but thickness of the fault gouge is set to 6 cm instead of the 3 mm in BS2B micro-structural model. In the second variant also fracture coating omitted (blue curves).* **Water residence time distribution:** Same as for Case A (Table 7-2). **WL/Q distribution:** Same as for Case A (Table 7-2).

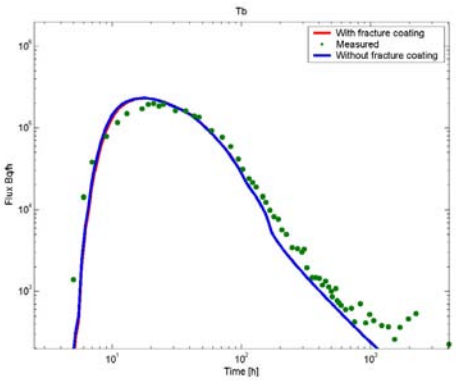

Tb-160

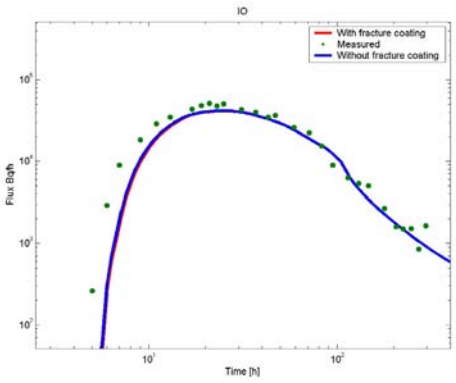

I-131

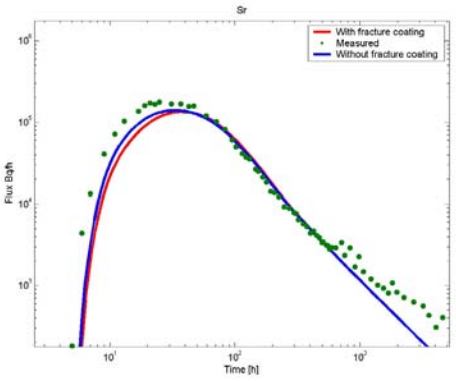

Sr-85

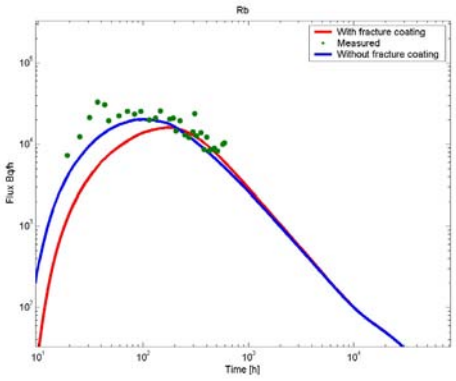

Rb-86

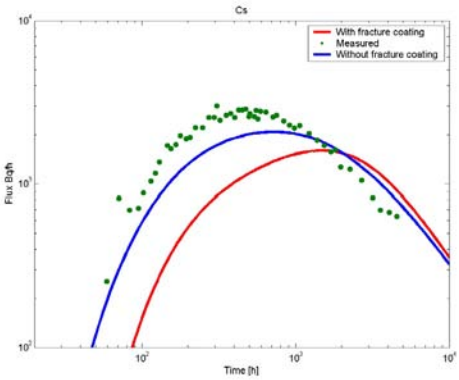

Cs-137

Figure 7-15. *Measured (dots) and calculated breakthrough curves for flow path I. The breakthrough curves have been calculated by retaining the flow field as measured by dilution experiments (CPT-3C). This entails the fault gouge to be the principal retention zone. Red lines show calculated breakthrough curves when all layers specified in the BS2B micro-structural model are taken into account. Blue lines show breakthrough curves for the case where the fracture coating is omitted. Alterations to the BS2B micro-structural model and the applied flow field are specified in Table 7-3.*

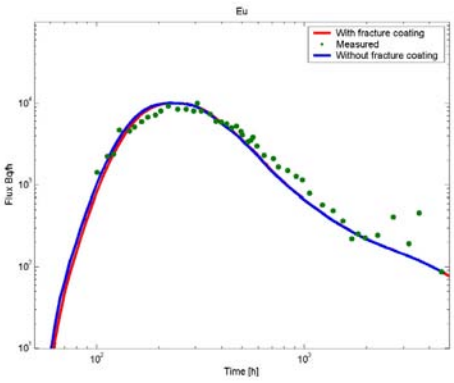

Eu-155

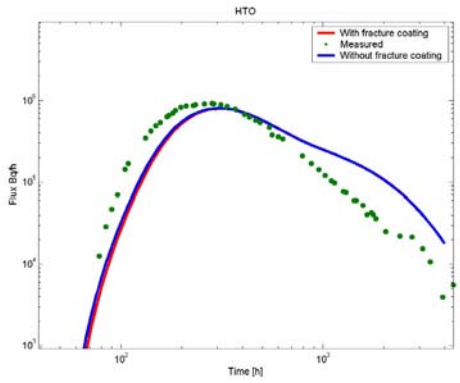

HTO

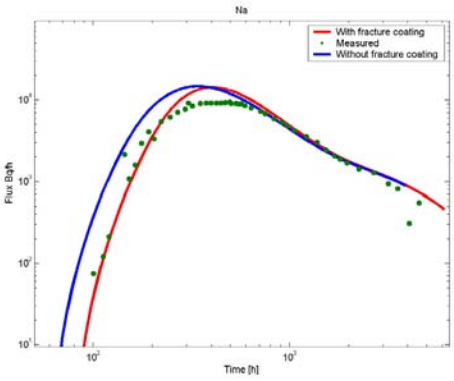

Na-22

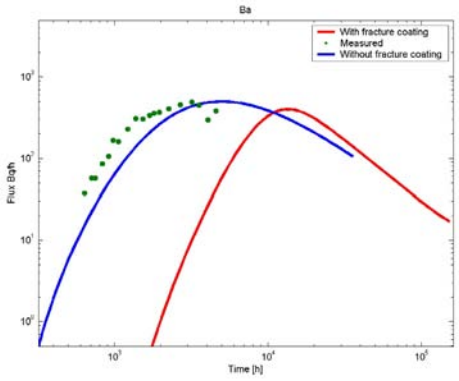

Ba-131

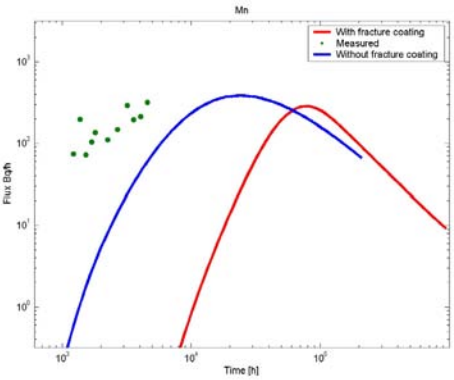

Mn-54

Figure 7-16. *Measured (dots) and calculated breakthrough curves for flow path II. Breakthrough curves have been calculated by retaining the flow field as measured by dilution experiments (CPT-3C). This entails the fault gouge to be the principal retention zone. Red lines show calculated breakthrough curves when all layers specified in the BS2B micro-structural model are taken into account. Blue lines show breakthrough curves for the case where the fracture coating is omitted. Alterations to the BS2B micro-structural model and the applied flow field are specified in Table 7-3.*

7.7 Results for the case of altered zone and intact rock only

Calculation of this model case is motivated by the observation that all breakthrough curves can be explained by unlimited matrix diffusion (i.e. unlimited in the time scale of the experiment). This can be seen for example from the fitted results in Figure 7-6 and Figure 7-7. In those figures the response function of unlimited matrix diffusion is used to model the BS2B experiment and the fit to the measured breakthrough curves is good. The response functions of these breakthrough curves are specified in Table 7-1.

The altered zone as the primary retention zone requires much stronger hydrodynamic control of the retention (WL/Q). The water residence time distribution is left unchanged but the average WL/Q is increased. In practice this means that the volume of the flow channel is fixed but the "geometry" of the flow channel is changed. The effective retention aperture is smaller and flow is distributed over a wider area to balance the weaker matrix diffusion properties of the altered zone (compared to e.g. fault gouge). In practice this requires quite large change to the flow geometry. For flow path I the average WL/Q needs to be increased by a factor of 40, and for flow path II by factor of 15. The resulting transport channel widths can be estimated by multiplying the widths of the transport channels given in Section 7.4 by these same factors. For flow path I this means a width of the transport channel that is about 8.3 m, and for flow path II about 10 m.

Table 7-4. Specification of the flow field and immobile pore space for the Case C.

Case C	**Immobile zone:** Same as for Case A (Table 7-2) *but fracture coating, fault gouge and cataclasite omitted.* **Water residence time distribution:** Same as for Case A (Table 7-2). **WL/Q distribution:** Flow path I: As in Case A (Table 7-2) *but 40 times larger values* Flow path II: As in Case A (Table 7-2) *but 15 times larger values*

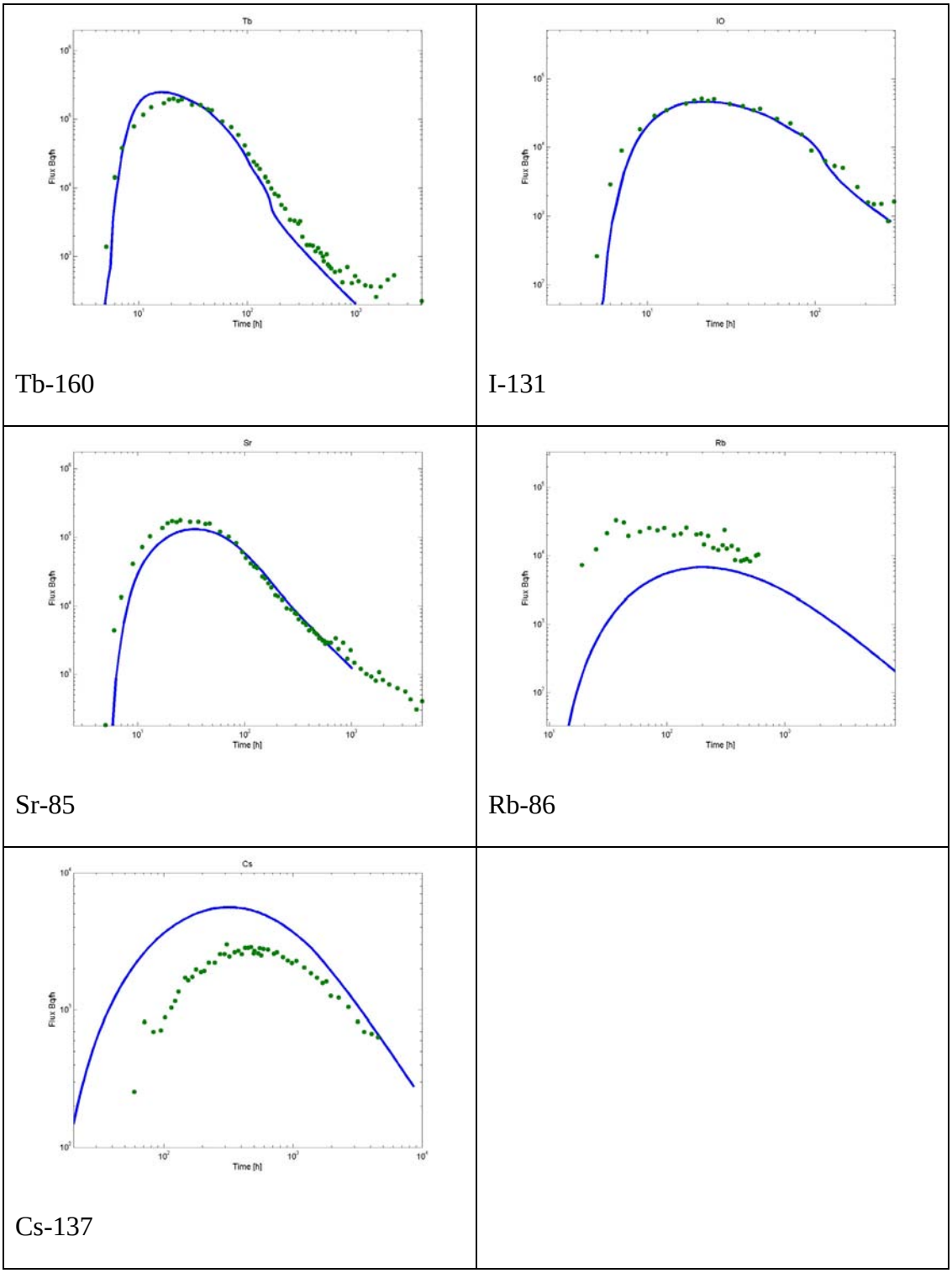

Figure 7-17. *Measured (dots) and calculated breakthrough curves for flow path I. Breakthrough curves were calculated considering the zone of altered rock to be principal retention zone. Alterations to the BS2B micro-structural model and the applied flow field are specified in Table 7-4.*

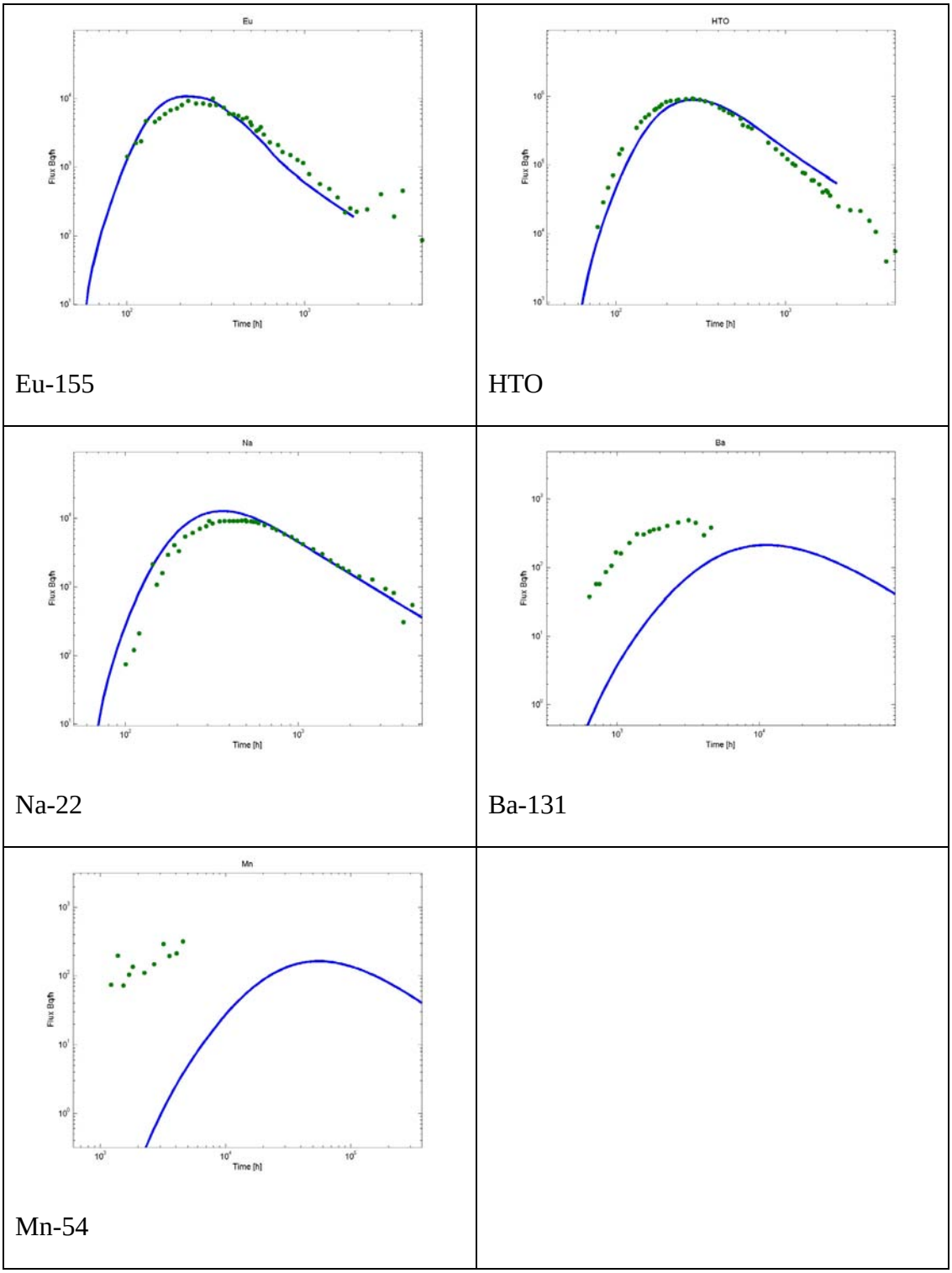

Figure 7-18. *Measured (dots) and calculated breakthrough curves for flow path II. Breakthrough curves were calculated considering the zone of altered rock to be principal retention zone. Alterations of BS2B micro-structural model and the applied flow field are specified in Table 7-4.*

8 Discussion

The evaluation applied in this report does not aim at calibration of the individual tracer K_d-values. The main emphasis has been put on the order of magnitude properties of the flow field and principal retention zones. This means that in the evaluation the K_d's have been left unchanged compared to the values that were applied in the predictions and are presented in Table 5-3. It would have been possible to obtain better fits for the sorbing tracers by fine-tuning the K_d's of the tracers.

One of the main findings of the evaluation is that according to the breakthrough curves it seems that the diffusion has taken place to an immobile zone that has a large volume. Matrix diffusion to a single unlimited immobile zone can explain the breakthrough curves very well (Section 7.3 and Table 7-1) and no clear signs of the limited matrix diffusion can be seen in the breakthrough curves, although it is impossible to distinguish retention in a fully saturated immobile zone from the equilibrium sorption.

Immobile zone retention properties along the flow path I and II can be directly compared by investigating the measured breakthrough curves. The fitted matrix diffusion parameter (*u*, c.f. Table 7-1) for the non-sorbing tracers is about 1.5 $h^{1/2}$ along the flow path I and from 8 $h^{1/2}$ to 11 $h^{1/2}$ along the flow path II. If the effective immobile zone retention properties are equivalent along both flow paths then the scaling of *u* should come solely from the scaling of the WL/Q. Statistics of the measured flow rates and roughly estimated path lengths (c.f. Section 3.1) are presented in Table 8-1. Table 8-1 presents a range of flow rates for the flow path II that is based on the estimate by Andersson et al. (2004) that due to the problems with the equipment the real flow rate at the injection location of the flow path II can be 10 times smaller than the measured value. Table 8-1 can be interpreted so that the matrix diffusion is 5-7 times stronger along the flow path II than it is along the flow path I, but this requires 30 times bigger hydrodynamic control of retention, i.e the effective immobile zone retention property is clearly stronger along flow path I, than along the flow path II. This is also reflected by the evaluation Case C, where the same immobile zone retention properties have been applied along both flow paths. The required enhancement for the WL/Q is clearly bigger for the flow path I, a factor of 40 compared to the factor of 15 for the flow path II.

Table 8-1. Comparison of the flow paths based on the rough estimates of the path lengths and flow rates. Based on Andersson et al. (2004) the lower limit of the given flow rates for the flow path II is considered more realistic.

	Length [m]	**Flow rate [ml/h]**	**WL/Q**	***u***
Flow Path I	20	68	-	-
Flow Path II	40	4.2-42	-	-
Ratio - FP II / FP I	2	0.062-0.62	3 – 30	5 – 7

The basic problem of the evaluation is that the retention depends both on the flow field and the material properties. Material properties are estimated on geological grounds and are presented as BS2B micro-structural model. The flow field is measured locally at the injection borehole sections in the CPT-3C tracer dilution experiment. Calculations using the BS2B micro-structural model show that the breakthrough curves cannot be explained by directly combining the micro-structural model and measured flow field (Section 7.5, evaluation calculations are based on the large flow rate, 42 ml/h, for the flow path II). Two alternatives of this base case were calculated. First, the flow field was kept unchanged and material properties were changed. It appeared that the thickness of the fault gouge should be increased to 6 cm, mainly because of the HTO breakthrough curve for the flow path II. In addition, the sorbing tracers indicate that the fracture coating does not exist, at least not in the way it is defined in the micro-structural model, or conceptualised in the evaluation model. The second alternative was calculated by changing both the flow field and micro-structural model. In that case the principal retention zone was comparable with altered rock. Fracture coating, fault gouge and cataclasite were omitted from this model. In this case the hydrodynamic control of retention (WL/Q) needs to be increased by a factor of 15 to 40. This corresponds to an effective transport aperture of about $4 \cdot 10^{-6}$ m for the flow path I and $3 \cdot 10^{-5}$ for the flow path II. If the geometry of the transport channel is represented by the average width of the channel applied in the WL/Q expression, then both channels need to be 8-10 m wide (they were 0.2 m to 0.7 m in the base case). The main features and outcome of the evaluation models are summarised in Table 8-2.

Table 8-2. Main features and outcome of the evaluation models.

Case	Features	Outcome
A	Immobile zones: BS2B micro-structural model. Flow field: CPT-3C dilution measurement flow rates.	Poor fits of the modelled BTC. Modelled BTC do not have correct tailings. Partial saturation of the centimetre scale immobile zones cause too narrow and high BTC peaks.
B	Immobile zones: BS2B micro-structural model + increased 6 cm thickness of gouge, one variant without fracture coating. Flow field: CPT-3C dilution measurement flow rates.	Acceptable fits to the measured BTC, especially without fracture coating. However, fits get worse for more sorbing tracers (note, Kd-values have not been fitted) Tailing of the HTO show still some signs of partial saturation of the fault gouge (the power-law tailing raises and then declines steeply).
C	Immobile zones: Only altered zone and intact rock as they have been defined in the micro-structural model. Flow field: CPT-3C dilution measurement flow rates decreased by a factor of 40 for the flow path I and a factor of 15 for the flow path II.	Acceptable fits to the measured BTC. Modelled BTC tailings follow experimental BTC tailings. Fits get worse for more sorbing tracers (note, Kd-values have not been fitted) The fit of Cs-137 BTC is particularly poor.

It is possible that for some of the tracers the tailing of the breakthrough curve is caused by processes that are not considered in this report. Section 7.2 shows that injection curve of Cs-137 deviates from the behaviour of the other tracers and also from what is expected to be the tracer dilution curve in the injection borehole section. Similar behaviour of the Cs (and also Rb) has been observed already in the TRUE Block Scale experiment. Andersson et al. (2002) noted that it is possible to explain the power-law behaviour of the Cs in the injection curves by applying non-linear sorption with a Freundlich isotherm.

Evaluation modelling results and findings of the direct investigation of the measured breakthrough curves are best summarised by the following observations:

- Effective immobile zone retention properties are clearly stronger for the flow path I. This supports the hypothesis that in the experimental time scale the effective immobile zone retention properties are stronger in the fault type feature than in the non-fault type feature
- The character of the unlimited matrix diffusion in the breakthrough curves indicates the major retention zone needs to be thick enough. Especially, this hold for the flow path II that exhibits more retention. Evaluation model Case C assigns the retention to altered zone (i.e. non-fault features) with about 15 times smaller flow rate than the base case. This supports the note by Andersson et al. (2004) that the dilution flow measurement at the injection location of the flow path II may show 10 times too large flow rate due to problems with the equipment.
- Evaluation has showed that very distinct layers of different materials at a centimeter scale (thickness of the material layer) should manifest themselves in the breakthrough curves of the non-sorbing tracers in the experimental time of the BS2B.
- The effective immobile zone retention property for the flow path I is in between the properties of the fault gouge and cataclasite. For the flow path II this property is close to that of the altered zone. This means that the flow path I is characterised by the fault type feature and the flow path II is characterised by the non-fault type feature.

It may be noted, that definitive evidence that matrix diffusion indeed has been an important retention process requires employment of different flow rates along the same flow path to show that the dynamic behaviour of the tracer retention follows the expected behaviour of the matrix diffusion.

9 Conclusions

Measured data do not show any major difference in the shape and tailing of the breakthrough curves for the Flow Path I and Flow Path II. Both flow paths show features that are typical of matrix diffusion, namely the $t^{-3/2}$-tailing of the breakthrough curves. In addition, the breakthrough curves show rather perfect match with a model of the unlimited matrix diffusion, which is also consistent with the sorption properties of the different tracers.

It is interesting that the unlimited matrix diffusion model explains so well the observed breakthrough curves. This indicates that the immobile layer causing the majority of the retention is quite thick, or that the contrast in the retention properties of the major immobile layers is small.

The main findings of the evaluation are here presented relative to the hypotheses tested by the sorbing BS2B experiment:

Hypothesis Ia) *Microstructural (i.e. detailed geological, mineralogical and geochemical) information can provide significant support for predicting transport of sorbing solutes at experimental time scales,*

Testing of this hypothesis by the predictive modelling failed somewhat because of the too high flow rates applied for the flow path II. However, direct investigation of the measured breakthrough curves and evaluation models supports this hypothesis. Flow path I seems to have a distinctively higher effective immobile zone retention property compared to flow path II. This can be assigned to the micro-structural model of the dominating fractures along the flow path I.

Hypothesis Ib) *Transport at experimental time scales is significantly different for faults (significant alteration, brecciation and fault gouge) and joints (with or without alteration), due to the indicated differences in microstructure and properties*

Evaluation shows that at experimental time scale it requires several times smaller flow rates along a joint as compared with a fault to attain the same retention. In this respect the evaluation supports this hypothesis. In addition, the evaluation seems to suggest that the effective retention property along a flow path, which starts from a non-fault fracture, is dominated by the non-fault fractures despite the fact that the flow path passes through a fault type fracture. The reason for is that the flow rates in the background fractures are much smaller than in the fault.

10 References

Andersson, P., Byegård, J., and Winberg, A., 2002. Final Report of the TRUE Block Scale Project. 2. Tracer Tests in the Block Scale. SKB Technical Report TR-02-14.

Andersson, P., Byegård, J., Nordqvist, R., and Wass, E., 2005. TRUE Block Scale Continuation. BS2B Tracer Tests with Sorbing Tracers. SKB, International Progress Report IPR-05-01.

Andersson, P., Gröhn, S., Nordqvist, R., and Wass, E., 2004: TRUE Block Scale Continuation, BS2 Pretests. Crosshole interference, dilution and tracer tests, CPT-1 CPT- 4. SKB International Progress Report IPR-04-25.

Byegård, J., and Tullborg, E.-L, 2004. Proposed sorption, porosity and diffusivity properties for the prediction modelling of the TRUE Block Scale Continuation BS2B sorbing tracer experiment. Technical Memorandum, version 0.1, July 8, 2004, TRUE Block Scale Continuation.

Cvetkovic, V. and R. Haggerty. Transport with multiple-rate exchange in disordered media. May 2002, Phys. Rev. E, Vol. 65, 051308.

Dershowitz, W., Winberg, A., Hermanson, J., Byegård, J., Tullborg, E.-L., Andersson, P. and Mazurek, M., 2003. Task 6C, A Semi-synthetic Model of Block Scale Conductivite Structures at the Äspö HRL. SKB, International Progress Report, IPR-03-13.

Matlab 2001, version 5.1.0.421, www.mathworks.com

Tullborg, E.-L., and Hermanson, J., 2004. Assignment of distribution of geological structure type, complexity and parameters of the micro-structural model applicable to the predictive modelling of the BS2B sorbing experiment. Technical Memorandum, March 25, 2004, TRUE Block Scale Continuation.

Winberg, A., 1997. Test plan for the TRUE Block Scale Experiment. Swedish Nuclear Fuel and Waste Management Company. Äspö Hard Rock Laboratory. International Cooperation Report ICR 97-02.